MÁSTERES de la UAM

Facultad de Ciencias /11-12

Máster en Química Teórica y Modelización Computacional

UAM
UNIVERSIDAD AUTONOMA
DE MADRID

Campus Internacional
excelencia UAM CSIC+

Computation of photoelectron and proton kinetic energy spectra in molecular ionization and dissociation

Rui Emanuel Ferreira da Silva

UAM EDICIONES

MASTER THESIS

COMPUTATION OF PHOTOELECTRON AND PROTON KINETIC ENERGY SPECTRA IN MOLECULAR IONIZATION AND DISSOCIATION

UA

UNIVERSIDAD AUTONOMA
DE MADRID

RUI EMANUEL FERREIRA DA SILVA

Supervised by Paula Rivière

Madrid, July 2011

À memória do meu avô Ferreirinha.

Acknowledgements

First of all I want to thanks to Paula Rivière. It was her comprehension, knowledge and patience that guide me in the hard path of research. For the long hours discussing science, teaching me the marvellous world of Atomic Physics, to teach me a lot of programming, to be the most comprehensive and kind person with respect to my sentimental need to go every weekend to Portugal. Thank you Paula.

Then I would like to thanks to Fernando Martín for the opportunity of working in such research group. For the confidence that puts on me by offering me the chance of proceed my PhD in Madrid. Because with his fantastic physical intuition I was able to understand results that for me at the beginning were like chinese characters.

I also need to say a word to Henri Bachau. Thanks for the help in my stage at Bordeaux and for the discussions that made the Resolvent Technique easier. Thanks also for the rides to the airport. I really appreciate your disponibility for even the silliest question.

I can not forget Fabrice Catoire. It was a pleasure to chat with someone so interesting and so brilliant. Thanks for introducing me to the wonderful world of the Resolvent Technique.

A word for the science manager of the group, Beatriz Martín, for her help in every bureaucratic task and for her disponibility and extreme competence.

A thanks to Professor Manuel Yañez, Professora Otilia Mó and Professor Manuel Alcamí for the organization of the EMTCCM.

I would like to thanks to all the people that have worked directly with the codes that I have used. Trying to not forgot anybody, I would like to thanks to Fernando Martín, Ignacio Sánchez, Jorge Fernández Hernández, Henri Bachau, Alicia Palacios, José Luis Sanz Vicario, Jhon-Fredy Pérez, Felipe Morales, Alberto González-Castrillo, Thomas Niederhausen and Paula Rivière.

I would like to thanks to all my colleagues of the master for having great times with them. A special thanks to Alberto Muzas, Humberto, Riccardo, Ana and Mai for the everyday friendship.

A thanks to all professors, students and post-docs of the Chemistry Department.

Agradeço aos meus amigos e família porque são o meu porto de abrigo.

Agradeço aos meus pais, que me deram uma vida sem igual e que todos os dias se esforçaram para que eu e as minhas irmãs tivessemos a melhor vida possível. Porque sem eles não seria quem sou, e sem eles não estaria aqui.

Agradeço à Mónica. Por ser quem é. Por ser o que é para mim. Por ser a razão do meu acordar, respirar e do meu viver.

Institutional support

The research leading to these results has received funding from the European Union Seventh Framework Programme (FP7/2007-2013) under grant agreement nº 264951.

Contents

List of Figures

Chapter 1

Introduction

In 1878, Muybridge took pictures of a horse during a gallop with a temporal resolution enough to see, in detail, the real movement of the legs of the horse. It was the beginning of a revolution in photography, but also in science. For the first time, we were able to take pictures to see in detail the motion of quick processes. The motivation of this work is of the same nature of Muybridge's work. Instead of understanding processes at the human scale, both temporal and spatial, we want to go further on the comprehension of the dynamics of atoms and molecules. To do that, we must use new methods that work under the typical atomic scale. A difficulty also arises from the fact that at the atomic and molecular scale the particles are no longer governed by the laws of Classical Mechanics, but Quantum Mechanics, since the typical action is of the order of $\hbar$.

It was back in the 1960's that a spot at the energy of the second harmonic was discovered. A crystal irradiated with an 800 nm intense laser was emitting light at 400 nm [1]. The field of non-linear optics was born. At the same time, it became possible to generate monochromatic light: laser science was born. Over the following decades, the laser science went into shorter and shorter time scales (of the order of a few femtoseconds). This was the beginning of ultrafast optics.

As stated before, to see a process in detail we must capture images under that time scale. With this idea in mind, experiments were done using ultrafast lasers on molecules to probe the nuclear motion, [2], since the typical time scale for it (the femtosecond (fs) domain) was now experimentally available. With Zewail's experiments a new field was opened, Femtochemistry. In this field people try to manipulate molecules, in order to track chemical reactions in real time and also to manipulate them. It has a huge technological potential in pharmaceutical and chemical industry.

In the 1990's, it was observed that atoms under an intense IR field irradiate photons with

energy equal to $E = (2N + 1)\,\omega$, where ω is the frequency of the IR pulse. These atomic spectra had some structure and its main feature was the cutoff at $I_p + 3.17U_p$, where $U_p = \frac{I}{4\omega^2}$ is the ponderomotive energy, that is the cycle averaged energy gain of a free electron in the electric field, I is the intensity of the field and ω its frequency.

This phenomenon was brilliantly explained by Corkum [3] with the so-called Three Step Model and latter by a quantum model [4] based on the Strong Field Approximation. One of the properties of the field irradiated by the atom was the low duration of the pulse, of the order of hundreds of attoseconds. This is the typical timescale of the electronic motion. The scientific community had then the chance to produce laser pulses that were able to probe the electronic motion in atoms and molecules. The field of Attophysics was created.

The study of electronic dynamics in atoms and molecules can be performed using pump-probe schemes with ultrashort laser pulses. Usually a pump pulse is used to induce some dynamics (typically an XUV pulse that induces ionization or dissociation) in the system and afterwards, a second pulse (probe) is used to probe that dynamics. In experiments, only the scattering states can be measured and the time evolution of the system cannot be followed. So how can we obtain a dynamical picture if only the asymptotic limit the system is accesible? The key parameter that can be adjusted experimentally is the time delay between both pulses, which can be controlled with attosecond precision. So our dynamical picture will be given by the analysis of the energy spectra of the fragments for different time delays.

In several recent experiments it was demonstrated that electronic motion can be controlled in an attosecond time scale using strong fs driving laser pulses [5]. This motion can also be used to measure directly the electric field of light [6], to produce XUV laser pulses with a few hundreds of attoseconds [7], and even to image electronic orbitals [8]. The importance and technological potential of this new field in physics and chemistry, which allows to access the internal dynamics of atoms and molecules, is growing every day.

New experimental techniques have been developed with this objective of visualizing and manipulating electronic dynamics in an attosecond time scale, by extracting the energy spectrum of particles ejected upon photoionization. Among these we find time-of-flight (TOF) techniques, velocity map imaging (VMI) [9] and Cold Target Recoil Ion Momentum Spectroscopy (COLTRIMS) [10]. These techniques can be combined with theoretical calculations to reveal the structural and dynamical information about molecules.

In the present work, we apply theoretical tools to study molecular processes under the presence of ultrashort pulses. To do so we solve the Time Dependent Schrödinger equation (TDSE), for whose resolution we use two main approaches. We can either solve it by discretizing the partial differential equations that our system obeys and solving them in a numerical grid, in the so-called

grid method, or expanding our wavefunction in a finite basis and calculating the couplings between the different states, and then propagating the TDSE, in the so-called spectral method.

The focus of this work is on molecular processes induced by ultrashort laser pulses. Since the TDSE is too complicated to solve for more than two electrons the study was done on simple molecules, H_2^+ and H_2, including the nuclear motion.

This Master Thesis is divided in four distinct parts. The starting point is a brief introduction (Chapter 2) to the laser-mater interaction formalism in non-relativistic quantum mechanics and the Hamiltonian of a diatomic molecule. In this Chapter the basic tools to deal with laser-matter interaction are given. The work developed in this thesis will be entirely done under the semi-classical approximation and within the dipole approximation using non-relativistic quantum mechanics.

In Chapter 3, a grid method to solve the TDSE for the H_2^+ molecule under the interaction of a laser pulse is presented. In this method, rotational effects are neglected and also the light is considered to be linearly polarized along the internuclear axis. This transforms our problem into a three dimensional problem, with two coordinates to describe the electronic motion and one to describe the nuclear motion. In this approach we solve the TDSE without assuming further assumptions, so we are working beyond the Born-Oppenheimer (BO) approximation. Even for a three dimensional grid the computational cost is huge. To calculate the momentum spectra, the Virtual Detector Method was applied, which allows a huge reduction on the size of our numerical box. In this Chapter, we also show some preliminary results. This method is still in development and it is aimed to work with very strong fields, since it is not restricted to the problem of a finite basis expansion as in spectral methods, and to study non-adiabatic effects.

In Chapter 4, we show a new theoretical method that we developed to extract kinetic energy spectra in molecules within a grid method, the Resolvent Technique for molecules. This technique is an extension of the Resolvent Technique that was already formulated for atoms [11]. It allows us to extract the doubly differential probability both in nuclear and electron energies. This combined observable is of great importance, since it allows to observe how energy is shared between the electron and the nuclei. We apply this new formalism in a grid calculation where the laser field is aligned with the internuclear axis, and we treat the electron with one coordinate and the nuclei with another one, in a reduced dimensionality model. We have studied one-photon absorption, where the energy of the photon is enough to directly induce ionization, the case when the photon energy couples resonantly the $1s\sigma_g$ and the $2p\sigma_u$ states, and the case of an IR (800 nm) laser when above threshold ionization (ATI) spectra can be observed. A publication on this topic is in preparation [12].

In Chapter 5, we focus on the study of autoionization of doubly excited states in the H_2 molecule, in particular, in the first series of resonant states, Q_1. To do so, we use a spectral method, under the BO approximation, that solves the TDSE. This method was already developed in the group [13–20]. We have used a pump-probe scheme consisting on an attosecond pulse train (APT) and a near-infrared (IR) pulse. The APT resonantly couples the molecular H_2 groundstate with the $^1\Sigma_u^+$ resonant states. The IR will probe the autoionization dynamics. This work has lead to a publication [21]. Another one on a similar topic is also submitted [22].

At the Conclusions we resume the main achievements of this master thesis and an outlook of future developments.

Chapter 2

Theoretical Background

"Physical concepts are free creations of the human mind, and are not, however it may seem, uniquely determined by the external world. In our endeavour to understand reality we are somewhat like a man trying to understand the mechanism of a closed watch. He sees the face and the moving hands, even hears its ticking, but he has no way of opening the case. If he is ingenious he may form some picture of a mechanism which could be responsible for all the things he observes, but he may never be quite sure his picture is the only one which could explain his observations. He will never be able to compare his picture with the real mechanism and he cannot even imagine the possibility or the meaning of such a comparison. But he certainly believes that, as his knowledge increases, his picture of reality will become simpler and simpler and will explain a wider and wider range of his sensuous impressions. He may also believe in the existence of the ideal limit of knowledge and that it is approached by the human mind. He may call this ideal limit the objective truth."

Albert Einstein and Leopold Infield

2.1 Laser-matter interaction

In this work we will deal with laser-matter interaction in diatomic molecules. Here we will briefly describe the equations that rule these interactions, Maxwell's equations, and the molecular Hamiltonian of such molecules.

2.1.1 Maxwell Equations

The Maxwell equations are a set of differential equations that unifies both electricity and magnetism, and they read (in SI units):

$$\nabla \cdot \boldsymbol{E}\left(\boldsymbol{r}, t\right) = \rho\left(\boldsymbol{r}, t\right)\varepsilon_0^{-1} \tag{2.1.1}$$

$$\nabla \cdot \boldsymbol{B}\left(\boldsymbol{r}, t\right) = 0 \tag{2.1.2}$$

$$\nabla \times \boldsymbol{E}\left(\boldsymbol{r}, t\right) = -\partial_t \boldsymbol{B}\left(\boldsymbol{r}, t\right) \tag{2.1.3}$$

$$\nabla \times \boldsymbol{B}\left(\boldsymbol{r}, t\right) = c^{-2}\partial_t \boldsymbol{E}\left(\boldsymbol{r}, t\right) + \varepsilon_0^{-1}c^{-2}\boldsymbol{j}\left(\boldsymbol{r}, t\right), \tag{2.1.4}$$

where $\boldsymbol{E}$ is the electric field, ρ is the charge density, ε_0 is the vacuum permittivity, $\boldsymbol{B}$ is the magnetic field, c is the speed of light and $\boldsymbol{j}$ is the current density.

In this way we can define the potential vector and the scalar potential and obtain both the electric field and the magnetic field from

$$\boldsymbol{B} = \nabla \times \boldsymbol{A} \tag{2.1.5}$$

$$\boldsymbol{E} = -\partial_t \boldsymbol{A} - \nabla U, \tag{2.1.6}$$

where $\boldsymbol{A}$ is the potential vector and U is the scalar potential.

Defining in this way the magnetic and electric fields, equations (2.1.2) and (2.1.3) are satisfied by definition. Replacing the previous relationships in the other two Maxwell equations, we obtain the dynamical equations for the vector and scalar potentials

$$\Delta U = -\frac{1}{\varepsilon_0}\rho - \nabla \cdot \partial_t \boldsymbol{A}, \tag{2.1.7}$$

$$\left(\frac{1}{c^2}\partial_t^2 - \Delta\right)\boldsymbol{A} = \varepsilon_0^{-1}c^{-2}\boldsymbol{j} - \nabla\left(\nabla \cdot \boldsymbol{A} + \frac{1}{c^2}\partial_t U\right). \tag{2.1.8}$$

There are infinite ways to define the same pair of electric and magnetic fields from the potentials. The transformation

$$\boldsymbol{A}' = \boldsymbol{A} + \nabla F \tag{2.1.9}$$

$$U' = U - \partial_t F, \tag{2.1.10}$$

being F a scalar function, does not change the electric and magnetic fields. This is called a *gauge transformation*. Since we have such a freedom to choose the potentials, we can impose conditions

to fix $\boldsymbol{A}$ and U. We will work on the most common used gauge in this field, the Coulomb gauge. This gauge imposes that the $\boldsymbol{A}$ vector field is a transverse field, that is $\nabla \cdot \boldsymbol{A} = 0$. In this gauge, we can show [23] that the scalar potential is just the Coulomb potential,

$$U\left(\boldsymbol{r}, t\right) = \frac{1}{4\pi\varepsilon_0} \int d^3 r' \frac{\rho\left(\boldsymbol{r}', t\right)}{\left|\boldsymbol{r} - \boldsymbol{r}'\right|}. \tag{2.1.11}$$

2.1.2   Particles in an electromagnetic field

Although the EM field is a quantum field, we will work on the semi-classical approximation where we consider the dynamics of the electrons and nuclei with quantum mechanics and we treat the EM field in a classical way. The justification for the latter is that, since a typical laser field has an intensity high enough to consider the density of photons very high, we can treat the field in a continuous way, and this will resemble to a classical field since the gain or loss of a photon is negligible.

The non-relativistic Hamiltonian for a system of particles in a classical electromagnetic field is [24]

$$\hat{H} = \sum_i \frac{1}{2m_i} \left(\hat{\boldsymbol{p}}_i - q_i \boldsymbol{A}\left(\hat{\boldsymbol{r}}_i, t\right)\right)^2 + \sum_i q_i U\left(\hat{\boldsymbol{r}}_i, t\right) \tag{2.1.12}$$

where m_i and q_i are the mass and charge of each particle.

Since we are working on the Coulomb gauge, we will have that $\sum_i q_i U = V_C$. Developing the first term we have that

$$\hat{H} = \sum_i \frac{1}{2m_i} \hat{\boldsymbol{p}}_i^2 - \sum_i \frac{q_i}{2m_i} \left(\hat{\boldsymbol{p}}_i \cdot \boldsymbol{A}\left(\hat{\boldsymbol{r}}_i, t\right) + \boldsymbol{A}\left(\hat{\boldsymbol{r}}_i, t\right) \cdot \hat{\boldsymbol{p}}_i\right) + \sum_i \frac{q_i^2}{2m_i} \boldsymbol{A}^2\left(\hat{\boldsymbol{r}}_i, t\right) + V_C. \tag{2.1.13}$$

The second term can be simplified since $\hat{\boldsymbol{p}}$ and $\boldsymbol{A}$ commute in the Coulomb gauge so we can rewrite the previous equation as

$$\hat{H} = \sum_i \frac{1}{2m_i} \hat{\boldsymbol{p}}_i^2 - \sum_i \frac{q_i}{m_i} \hat{\boldsymbol{p}}_i \cdot \boldsymbol{A}\left(\hat{\boldsymbol{r}}_i, t\right) + \sum_i \frac{q_i^2}{2m_i} \boldsymbol{A}^2\left(\hat{\boldsymbol{r}}_i, t\right) + V_C. \tag{2.1.14}$$

This Hamiltonian has two interaction terms with the field, one linear and another one quadratical.

A very used approximation is the dipole approximation or long-wavelength approximation. In this approximation we suppose that the vector potential does not depend on spatial coordinates, but only on time. The validity of this approximation depends on the wavelength of the field. Since the spatial extension of an atom is of the order of the Bohr radius, this approach will be valid for

wavelengths of the field which are much bigger than the Bohr radius. The resulting Hamiltonian is

$$\hat{H} = \sum_i \frac{1}{2m_i} \hat{\boldsymbol{p}}_i^2 - \sum_i \frac{q_i}{m_i} \hat{\boldsymbol{p}}_i \cdot \boldsymbol{A}\left(\boldsymbol{r}_0, t\right) + \sum_i \frac{q_i^2}{2m_i} \boldsymbol{A}^2\left(\boldsymbol{r}_0, t\right) + V_C \qquad (2.1.15)$$

where $\boldsymbol{r}_0$ is the atomic position. The vector potential does no longer depend on the position operator. The quadratic term is only a time-dependent scalar and it will not couple different states, so our interaction term can be written as

$$\hat{H}_{int} = -\sum_i \frac{q_i}{m_i} \hat{\boldsymbol{p}}_i \cdot \boldsymbol{A}\left(\boldsymbol{r}_0, t\right). \qquad (2.1.16)$$

The interaction term in (2.1.16) is written in the so-called velocity gauge.

There is another way to express the interaction term. Using the Göppert-Mayer gauge or length gauge, and defining $F\left(\boldsymbol{r}, t\right) = -\left(\boldsymbol{r} - \boldsymbol{r}_0\right) \cdot \boldsymbol{A}\left(\boldsymbol{r}_0, t\right)$ we will get

$$\boldsymbol{A}' = 0 \qquad (2.1.17)$$

$$U' = U + \left(\boldsymbol{r} - \boldsymbol{r}_0\right) \cdot \partial_t \boldsymbol{A}\left(\boldsymbol{r}_0, t\right) = U - \left(\boldsymbol{r} - \boldsymbol{r}_0\right) \cdot \boldsymbol{E}\left(\boldsymbol{r}_0, t\right) \qquad (2.1.18)$$

recalling that $\boldsymbol{E} = -\partial_t \boldsymbol{A}$. Replacing the new potentials in the Hamiltonian

$$\hat{H} = \sum_i \frac{1}{2m_i} \hat{\boldsymbol{p}}_i^2 + V_{Coulomb} + \hat{H}_{int}(t), \qquad (2.1.19)$$

$$\hat{H}_{int}(t) = -\sum_i q_i \left(\hat{\boldsymbol{r}}_i - \boldsymbol{r}_0\right) \cdot \boldsymbol{E}\left(\boldsymbol{r}_0, t\right). \qquad (2.1.20)$$

Defining the dipole operator as $\hat{\boldsymbol{D}} = \sum_i q_i \left(\hat{\boldsymbol{r}}_i - \boldsymbol{r}_0\right)$, the interaction Hamiltonian in the length gauge can be written as

$$\hat{H}_{int} = -\hat{\boldsymbol{D}} \cdot \boldsymbol{E}\left(\boldsymbol{r}_0, t\right) \qquad (2.1.21)$$

The two gauges presented here are the most common gauges used in strong field physics. They are formally equivalent, since the wave function is gauge invariant. However, when numerical calculations are performed, only on the exact limit they coincide. In each case there must be evaluated which gauge is more convenient.

2.1.3 Molecular Hamiltonian for diatomic molecules

In this treatment we will neglect all relativistic effects including the spin dependent interaction

terms.

For a general molecule with N nuclei and n electrons, $\boldsymbol{r}_i$ denoting the coordinates of each electron and $\boldsymbol{R}_i$ denoting the coordinates of each nucleus, the Molecular Hamiltonian in the Space-Fixed Coordinate System (SFCS) reads

$$
\begin{aligned}
\hat{H} &= \hat{T}_e + \hat{T}_N + \hat{V}_{NN} + \hat{V}_{eN} + \hat{V}_{ee} \\
&= \sum_{i=1}^{n} -\frac{\hbar^2}{2m_e}\nabla^2_{\boldsymbol{r}_i} + \sum_{i=1}^{N} -\frac{\hbar^2}{2M_i}\nabla^2_{\boldsymbol{R}_i} + \sum_{i=1}^{N}\sum_{j=i+1}^{N} \frac{Z_i Z_j e^2}{4\pi\varepsilon_0 |\boldsymbol{R}_i - \boldsymbol{R}_j|} \\
&\quad + \sum_{i=1}^{N}\sum_{j=1}^{n} \frac{-Z_i e^2}{4\pi\varepsilon_0 |\boldsymbol{R}_i - \boldsymbol{r}_j|} + \sum_{i=1}^{n}\sum_{j=i+1}^{n} \frac{e^2}{4\pi\varepsilon_0 |\boldsymbol{r}_i - \boldsymbol{r}_j|}
\end{aligned}
\tag{2.1.22}
$$

where $\hat{T}_e$ is the kinetic energy operator for the electrons, $\hat{T}_N$ is the kinetic energy operator for the nuclei, $\hat{V}_{NN}$ is the electrostatic potential between the nuclei, $\hat{V}_{ee}$ is the electrostatic potential between the electrons, $\hat{V}_{eN}$ is the electrostatic potential between nuclei and electrons, m_e is the mass of the electron, M_i is the mass of the ith nucleus, e is the elementary charge of the electron and $-Z_i e$ is the charge of the ith nucleus.

In most cases, we can separate the motion of the center of mass, saving three degrees of freedom. For a diatomic molecule, eq. (2.1.22) takes the following form

$$
\hat{H} = -\frac{\hbar^2}{2M_a}\nabla^2_a - \frac{\hbar^2}{2M_b}\nabla^2_b + \sum_{i=1}^{n} -\frac{\hbar^2}{2m_e}\nabla^2_{\boldsymbol{r}_{i'}} + V
\tag{2.1.23}
$$

where V includes all the Coulomb interaction terms, M_a is the mass of one of the nucleus and M_b is the mass of the other nucleus.

Now we want to introduce a new set of coordinates, written as a function of the old coordinates. We start by defining the position vector of the center-of-mass of the system, $\boldsymbol{R}_{CM}$. Having it selected, we can now introduce the vector $\boldsymbol{R}$, which is the relative coordinate of the molecular axis. The new electronic coordinates will be defined with respect to the geometric center of the molecule (instead of being defined with respect to the center-of-mass) as $\boldsymbol{r}_i = \boldsymbol{r}_{i'} - \frac{1}{2}(\boldsymbol{R}_a + \boldsymbol{R}_b)$. The equations that define this new coordinates are

$$
\boldsymbol{R}_{CM} = \frac{1}{M}\left(M_a\boldsymbol{R}_a + M_b\boldsymbol{R}_b + \sum_{i=1}^{n} m_e\boldsymbol{r}_{i'}\right)
\tag{2.1.24}
$$

$$
\boldsymbol{R} = \boldsymbol{R}_a - \boldsymbol{R}_b
\tag{2.1.25}
$$

$$
\boldsymbol{r}_i = \boldsymbol{r}_{i'} - \frac{1}{2}(\boldsymbol{R}_a + \boldsymbol{R}_b)
\tag{2.1.26}
$$

where $M = M_a + M_b + n\,m_e$ is the total mass of the system. In this new coordinates it is easy to see that

$$
\nabla_{\boldsymbol{R_a}} = \frac{M_a}{M}\nabla_{\boldsymbol{R_{CM}}} + \nabla_{\boldsymbol{R}} - \frac{1}{2}\sum_{i=1}^{n}\nabla_{\boldsymbol{r_i}}
$$

$$
\nabla_{\boldsymbol{R_b}} = \frac{M_b}{M}\nabla_{\boldsymbol{R_{CM}}} - \nabla_{\boldsymbol{R}} - \frac{1}{2}\sum_{i=1}^{n}\nabla_{\boldsymbol{r_i}}
$$

$$
\nabla_{\boldsymbol{r_{i'}}} = \frac{m_e}{M}\nabla_{\boldsymbol{R}} + \nabla_{\boldsymbol{r_i}}
$$

and replacing the previous relationships into eq. (2.1.23) we obtain

$$
\hat{H} = -\frac{\hbar^2}{2M}\nabla^2_{\boldsymbol{R_{CM}}} + \hat{H}_0 + \hat{H}' \tag{2.1.27}
$$

where the first term is the center-of-mass kinetic energy operator. The second term is the electronic Hamiltonian and it has the following form

$$
\hat{H}_0 = -\sum_{i=1}^{n}\frac{\hbar^2}{2m_e}\nabla_i^2 + V \tag{2.1.28}
$$

and

$$
\hat{H}' = -\frac{\hbar^2}{2\mu}\nabla^2_{\boldsymbol{R}} + \hat{H}'' \tag{2.1.29}
$$

$$
\hat{H}'' = -\frac{\hbar^2}{8\mu}\left(\sum_{i=1}^{n}\nabla_{\boldsymbol{r_i}}\right)^2 - \frac{\hbar^2}{2}\left(\frac{1}{M_a} - \frac{1}{M_b}\right)\nabla_{\boldsymbol{R}}\sum_{i=1}^{n}\nabla_{\boldsymbol{r_i}} \tag{2.1.30}
$$

where $-\frac{\hbar^2}{2\mu}\nabla^2_{\boldsymbol{R}}$ is the kinetic energy operator of the reduced nuclei mass, and $\frac{1}{\mu} = \frac{1}{M_a} + \frac{1}{M_b}$. The term $\hat{H}''$ is usually neglected and couples the electronic and nuclear motions.

Chapter 3

Detection of observables in a grid method: the H_2^+ molecule

"To those who do not know mathematics it is difficult to get across a real feeling as to the beauty, the deepest beauty, of nature... If you want to learn about nature, to appreciate nature, it is necessary to understand the language that she speaks in."

Richard Feynman

3.1 Theory

In this Chapter we present a method to solve the TDSE in a numerical grid for the H_2^+ molecule interacting with a laser field linearly polarized along the internuclear axis. The method neglects rotational effects and takes advantage of the symmetry of the problem by expressing the electron coordinates in cylindrical coordinates. We have implemented a three-dimensional Virtual Detector Method for the extraction of the kinetic energy spectra.

3.1.1 Hamiltonian

In section 2.1.3, we have found the general expression of the molecular Hamiltonian for a diatomic molecule in the body fixed reference frame. In the specific case of the H_2^+, we can write

the full non-relativistic field free Hamiltonian (in atomic units) as

$$\hat{H}_0 = -\frac{1}{2M}\nabla_{\boldsymbol{R}}^2 - \frac{1}{2\mu_e}\nabla_{\boldsymbol{r}}^2 + \frac{1}{|\boldsymbol{R}|} - \frac{1}{\left|\boldsymbol{r}+\frac{\boldsymbol{R}}{2}\right|} - \frac{1}{\left|\boldsymbol{r}-\frac{\boldsymbol{R}}{2}\right|} \tag{3.1.1}$$

where $M = 918.076$ is the reduced mass of the two nuclei, and $\mu_e = 4M/\left(4M+1\right)$ is the reduced mass of the electron.

In order to treat the laser-molecule interaction we need to add the interaction term in the Hamiltonian. We will restrict our study to linear polarized light along the molecular axis (we will take the electric field along the z axis) and we will also neglect any rotational effects. This approach has an experimental motivation and also a computational motivation. Reducing the dimensionality of our problem from a 6-D problem to a 3-D problem turns our problem simpler and not so computationally expensive. There are also experimental methods that can select only aligned molecules, making our results comparable with experiments [25–29].

Neglecting all rotational effects fixes the orientation of the internuclear axis (see fig. 3.1). Expressing the $\boldsymbol{r}$ coordinate in cylindrical coordinates (ρ, z, ϕ) with the origin in the middle of our molecular axis, z parallel to the internuclear axis, and making R the vibrational coordinate, we obtain the following Hamiltonian

$$\begin{aligned}\hat{H}_0 &= -\frac{1}{2M}\frac{\partial^2}{\partial R^2} - \frac{1}{2\mu_e}\left(\frac{\partial^2}{\partial \rho^2} + \frac{1}{\rho}\frac{\partial}{\partial \rho} + \frac{\partial^2}{\partial z^2} + \frac{1}{\rho^2}\frac{\partial^2}{\partial \phi^2}\right) \\ &\quad + \frac{1}{R} - \frac{1}{\sqrt{\rho^2 + \left(z+\frac{R}{2}\right)}} - \frac{1}{\sqrt{\rho^2 + \left(z-\frac{R}{2}\right)}}.\end{aligned} \tag{3.1.2}$$

The Hamiltonian commutes with $\hat{L}_z = -i\frac{\partial}{\partial\phi}$, so the eigenfunctions of the Hamiltonian can be written as $\Phi\left(R, \rho, z, \phi\right) = \Psi\left(R, \rho, z\right)e^{im\phi}$, being m an integer that is an eigenvalue of the $\hat{L}_z$ operator. The nuclear dipole moment in the body-fixed reference frame is zero, so in the dipole approximation and in the length gauge, our interaction Hamiltonian reads

$$\hat{V}_L\left(t\right) = +zE\left(t\right). \tag{3.1.3}$$

The molecular groundstate has $m = 0$ and knowing that the laser field, which is linearly polarized, can not couple two states with different m, there is no dependence on the azimuthal angle, so the $\frac{1}{\rho^2}\frac{\partial^2}{\partial\phi^2}$ term in the Hamiltonian disappears. We will define our normalization condition
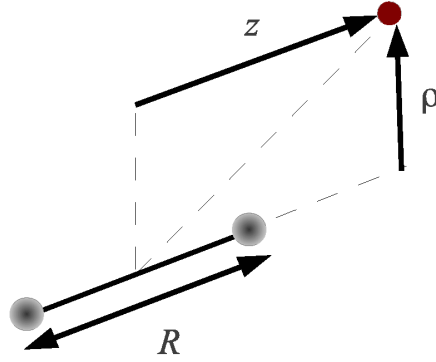
Figure 3.1: Coordinate system used to describe the H_2^+ system.

as $\iiint dR\rho d\rho dz \, |\Psi(R, \rho, z)|^2 = 1$. The time-dependent Hamiltonian will then be written as

$$\hat{H}(t) = \hat{T}_R + \hat{T}_z + \hat{T}_\rho + \hat{V}_C + \hat{V}_L(t) \tag{3.1.4}$$

$$\hat{T}_R = -\frac{1}{2M}\frac{\partial^2}{\partial R^2} \tag{3.1.5}$$

$$\hat{T}_z = -\frac{1}{2\mu_e}\frac{\partial^2}{\partial z^2} \tag{3.1.6}$$

$$\hat{T}_\rho = -\frac{1}{2\mu_e}\left(\frac{\partial^2}{\partial \rho^2} + \frac{1}{\rho}\frac{\partial}{\partial \rho}\right) \tag{3.1.7}$$

$$\hat{V}_C = \frac{1}{R} - \frac{1}{\sqrt{\rho^2 + \left(z + \frac{R}{2}\right)}} - \frac{1}{\sqrt{\rho^2 + \left(z - \frac{R}{2}\right)}}. \tag{3.1.8}$$

where $\hat{T}_R$, $\hat{T}_z$, $\hat{T}_\rho$ are the kinetic energy operator associated to the R, z and ρ coordinates, respectively, and $\hat{V}_C$ is the Coulomb interaction term between the particles.

3.1.2 Time-Dependent Schrödinger Equation

We start with the Schrödinger equation.

$$i\frac{\partial}{\partial t}\Psi(\boldsymbol{r}, t) = \hat{H}(t)\Psi(\boldsymbol{r}, t) \tag{3.1.9}$$

A formal integration of (3.1.9) gives [30]

$$\Psi\left(\boldsymbol{r}, t\right) = \hat{P} \exp\left[-i \int_{t_0}^{t} dt' \hat{H}\left(t'\right)\right] \Psi\left(\boldsymbol{r}, t_0\right) \tag{3.1.10}$$

where $\hat{P}$ is the Dyson time-ordering operator. Eq.(3.1.10) is another way to write the TDSE, but the time-ordering operator it is very difficult to evaluate. For some cases the Dyson operator becomes a more feasible object, such as in a time-independent Hamiltonian where eq. (3.1.10) becomes

$$\Psi\left(\boldsymbol{r}, t\right) = \exp\left[-i\left(t - t_0\right) \hat{H}\right] \Psi\left(\boldsymbol{r}, t_0\right). \tag{3.1.11}$$

For an interval $[t, t + \Delta t]$ where Δt is a very small time step, the integral in the equation (3.1.10) can be approximated by $\hat{H}\left(t + \Delta t/2\right) \Delta t$. In this case

$$\Psi\left(\boldsymbol{r}, t + \Delta t\right) = \exp\left(-i\Delta t \hat{H}\left(t + \Delta t/2\right)\right) \Psi\left(\boldsymbol{r}, t\right) \tag{3.1.12}$$

But how can we evaluate the exponential of the Hamiltonian? We can in principle, diagonalize the Hamiltonian, and the exponential of the Hamiltonian would be straightforward[1], but since we want to work on a numerical grid, where we explicitly avoid the diagonalization of our Hamiltonian, we must use another method. We will apply the Crank-Nicholson method.

3.1.3 Crank-Nicholson Method

Our first approach to the question that arose in the previous section would be to expand the exponential in a Taylor series, truncating the series at a certain order. However, we will not expand in a Taylor series but into a Padé Approximant. The problem of the expansion in a Taylor series is the fact that the approximated exponential operator would not be unitary. In fact, it can be easily verified that in first order, $\left(\hat{1} - i\Delta t \hat{H}\right)\left(\hat{1} - i\Delta t \hat{H}\right)^{\dagger} \neq \hat{1}$.

The Padé Approximant is a rational approximation to a function. In general, a function $f\left(z\right)$ can be written as

$$f\left(z\right) = \frac{P_n\left(z\right)}{Q_m(z)} + \mathcal{O}\left(z^{n+m+1}\right) \tag{3.1.13}$$

where P_n and Q_m are two polynomials of order n and m. Evaluating the exponential with $n = 1$

---

[1]The exponential of a diagonal matrix is a diagonal matrix whose terms are the exponentials of the diagonal terms of the original matrix.

and $m = 1$ we get

$$\exp(z) = \frac{2+z}{2-z} + \mathcal{O}(z^3).$$

(3.1.14)

Applying this to equation (3.1.12), we obtain

$$\Psi(\boldsymbol{r}, t + \Delta t) = \left(\frac{1 - i\hat{H}\Delta t/2}{1 + i\hat{H}\Delta t/2}\right)\Psi(\boldsymbol{r}, t)$$

(3.1.15)

where $\hat{H}$ is evaluated at $t + \Delta t/2$. With this expansion we introduce an error $\mathcal{O}(\Delta t^3)$. It is important to notice that this propagator will now be unitary, since $\left(\frac{1-i\hat{H}\Delta t/2}{1+i\hat{H}\Delta t/2}\right)\left(\frac{1-i\hat{H}\Delta t/2}{1+i\hat{H}\Delta t/2}\right)^{\dagger} = \hat{1}$. To calculate $\Psi(\boldsymbol{r}, t + \Delta t)$ we can write eq. (3.1.15) in the following form

$$\left(1 + i\hat{H}\Delta t/2\right)\Psi(\boldsymbol{r}, t + \Delta t) = \left(1 - i\hat{H}\Delta t/2\right)\Psi(\boldsymbol{r}, t)$$

(3.1.16)

and in a numerical grid this will become a set of linear equations. Since the complexity of this problem increases with the dimensionality of the problem we can separate the propagation of each time step into pieces, in the so-called Split-Operator Method.

3.1.4 Split-Operator Method

Making use of eq. (3.1.15) without further approximations requires the solution of a linear set of N equations, that in general does not scale linearly with N. We know that for the one-dimensional case, the kinetic energy operator, in a numerical grid and applying a three-point difference scheme, can be expressed as a tridiagonal matrix. The potential operator is diagonal and the resulting Hamiltonian is a tridiagonal matrix. This can lead to a substantial reduction of computational effort, since there is a very efficient algorithm to solve tridiagonal systems of equations that scales with N. The algorithm is known as the tridiagonal matrix algorithm or Thomas algorithm.

In order to decrease the computational effort, it would be enough to split the propagator into one-dimensional propagators. We start by looking at (3.1.12) and expressing the Hamiltonian as the sum of an kinetic energy operator $\hat{T}$ and a potential energy operator $\hat{V}$. The Zassenhaus formula [31] provides a way to calculate the exponential of the sum of two or three operators

$$e^{t(\hat{X}+\hat{Y})} = e^{t\hat{X}}e^{t\hat{Y}}e^{-\frac{t^2}{2}[\hat{X},\hat{Y}]}e^{\mathcal{O}(t^3)}$$

(3.1.17)

$$e^{t(\hat{X}+\hat{Y}+\hat{Z})} = e^{t\hat{X}}e^{t\hat{Y}}e^{t\hat{Z}}e^{-\frac{t^2}{2}([\hat{X},\hat{Y}]+[\hat{Y},\hat{Z}]+[\hat{X},\hat{Z}])}e^{\mathcal{O}(t^3)}$$

(3.1.18)

If we replace $e^{-i\Delta t(\hat{T}+\hat{V})}$ by $e^{-i\Delta t\hat{T}}e^{-i\Delta t\hat{V}}$, we are making an error of $\mathcal{O}(\Delta t^2)$. Instead if we use

$$e^{-i\Delta t(\hat{V}/2+\hat{T}+\hat{V}/2)} \rightarrow e^{-i\frac{\Delta t}{2}\hat{V}}e^{-i\Delta t\hat{T}}e^{-i\frac{\Delta t}{2}\hat{V}} \tag{3.1.19}$$

since $\left[\hat{V}/2,\hat{T}\right] + \left[\hat{T},\hat{V}/2\right] + \left[\hat{V}/2,\hat{V}/2\right] = 0$, we will only make an error of $\mathcal{O}(\Delta t^3)$. Since the kinetic energy operator, in our case, is $\hat{T} = \hat{T}_R + \hat{T}_\rho + \hat{T}_z$ and since each one of the kinetic energy operators commutes with the others, we can factorize the exponential without making an additional approximation. In this way, our propagator will be written as

$$e^{-i\frac{\Delta t}{2}\hat{V}}e^{-i\Delta t\hat{T}_R}e^{-i\Delta t\hat{T}_\rho}e^{-i\Delta t\hat{T}_z}e^{-i\frac{\Delta t}{2}\hat{V}} \tag{3.1.20}$$

We know that the time scale for the electronic motion is shorter than the timescale for the motion of the nuclei, so we can take two time steps for the propagation: Δt_{elec} for propagating the potential and the electronic kinetic energy operator and $\Delta t_{nuc} = k\Delta t_{elec}$ for propagating the nuclear kinetic energy operator (in particular, we use $k = 10$). Every exponential is evaluated using the Cranck-Nicholson method. The explicit form of each kinetic energy operator will be explained in the next section.

3.1.5 Kinetic and potential energy operators in a non-uniform grid

The treatment given in this section is based on [32]. The time-independent Schrödinger equation can be formulated on a variational way. We know that the eigenstates of an Hamiltonian can be obtained by minimizing the energy functional, i.e.

$$\frac{\delta E[\Psi]}{\delta\Psi} = 0 \tag{3.1.21}$$

$$E[\Psi] = \frac{\langle\Psi|\hat{H}|\Psi\rangle}{\langle\Psi|\Psi\rangle}, \tag{3.1.22}$$

and for a one-dimensional case we have

$$E[\Psi] = \frac{\int \left(\frac{1}{2\mu}\frac{d\Psi^*}{dx}\frac{d\Psi}{dx} + V\right)\xi(x)\,dx}{\int \Psi^*\Psi\rho(x)\,dx} \tag{3.1.23}$$

where μ is the mass of the particle and $\xi(x)\,dx$ is the volume element. It must be noticed that equation (3.1.23) can be simply generalized to the multi-dimensional case. To keep it in a simpler

and clear way, the following analysis will be done for the one-dimensional case.

To discretize this equation we will replace any integral by the midpoint rule

$$\int f(x)\,dx \rightarrow \sum_{i=1}^{N} f(x_i)\left(x_{i+(1/2)} - x_{i-(1/2)}\right) \tag{3.1.24}$$

and the derivatives by the central differencing scheme

$$\left.\frac{df}{dx}\right|_{x_i} \rightarrow \frac{f_{i+(1/2)} - f_{i-(1/2)}}{x_{i+(1/2)} - x_{i-(1/2)}}. \tag{3.1.25}$$

In this treatment we will work with an arbitrary grid. The variational principle can also be written in the following form

$$\frac{\partial E[\Psi]}{\partial \Psi_j^*} = 0. \tag{3.1.26}$$

Substituting eqs. (3.1.24) and (3.1.25) in eq. (3.1.23), we obtain

$$\frac{1}{2\mu}\left[\frac{\Psi_j - \Psi_{j-1}}{x_j - x_{j-1}}\xi_{j-(1/2)} - \frac{\Psi_{j+1} - \Psi_j}{x_{j+1} - x_j}\xi_{j+(1/2)}\right] + V_j\Psi_j\xi_j\left(x_{j+(1/2)} - x_{j-(1/2)}\right) = \tag{3.1.27}$$
$$E\Psi_j\xi_j\left(x_{j+(1/2)} - x_{j-(1/2)}\right)$$

where j is the spatial index. Rewriting as a matrix equation we get

$$\boldsymbol{H}\vec{\Psi} = E\boldsymbol{S}\vec{\Psi} \tag{3.1.28}$$

where $\boldsymbol{H}$ is the Hamiltonian matrix and $\boldsymbol{S}$ is the overlap matrix. The wavefunction is written as $\vec{\Psi}$ to remark the fact that after discretization we can express the wavefunction as a column vector. The Hamiltonian matrix is a tridiagonal, non-Hermitian matrix. The overlap matrix is a diagonal matrix.

We must impose boundary conditions. In this case our boundary conditions can be the continuity or the differentiability of the wavefunction at the boundaries. If we impose that the wavefunction must be zero at the boundaries, we then must set Ψ_0 (and Ψ_{N+1}) as zero. No other changes in the matrix are needed. On the other hand, if we impose that the derivative of the wavefunction at the boundaries is zero we must impose that $\Psi_0 = \Psi_1$ (or $\Psi_{N+1} = \Psi_N$). This requires that a $\frac{1}{2\mu}\frac{\xi_{1/2}}{x_1 - x_o}$ term should be subtracted from the first diagonal element of the Hamiltonian matrix. A similar term must be subtracted of the last diagonal element of the Hamiltonian. We will choose this last option for the boundary conditions.

We have arrived to a generalized eigenvalue problem. We can rewrite the overlap matrix as

$$\boldsymbol{S} = \boldsymbol{L}\boldsymbol{L}^T \tag{3.1.29}$$

and since $\boldsymbol{S}$ is a diagonal matrix we obtain

$$L_i = \sqrt{S_i}. \tag{3.1.30}$$

We can transform the Hamiltonian matrix and the wavefunction accordingly and transform the generalized eigenvalue problem into a standard eigenvalue problem,

$$\boldsymbol{H}' = \boldsymbol{L}^{-1}\boldsymbol{H}\boldsymbol{L}^{-T} \tag{3.1.31}$$
$$\vec{\Psi}' = \boldsymbol{L}^T\vec{\Psi} \tag{3.1.32}$$
$$\boldsymbol{H}'\vec{\Psi}' = E\vec{\Psi}' \tag{3.1.33}$$

This transformation will produce a Hermitian Hamiltonian. We can write explicitly the value of the transformed Hamiltonian. It will be a tridiagonal matrix, just like before the transformation. The diagonal elements of the new Hamiltonian will be

$$H'_{ii} = \frac{1}{2\mu}\left[\frac{1}{x_i - x_{i-1}}\xi_{i-(1/2)} - \frac{1}{x_{i+1} - x_i}\xi_{i+(1/2)}\right]\frac{1}{\xi_i\left(x_{i+(1/2)} - x_{i-(1/2)}\right)} + V_i, \tag{3.1.34}$$

and the non-diagonal elements of the matrix will be

$$H'_{i,i+1} = -\frac{1}{2\mu}\frac{\xi_{i+(1/2)}}{(x_{i+1} - x_i)\sqrt{\xi_i\left(x_{i+(1/2)} - x_{i-(1/2)}\right)\xi_{i+1}\left(x_{i+(3/2)} - x_{i+(1/2)}\right)}} + V_i \tag{3.1.35}$$

where the other terms can be obtained by the symmetry of the $\boldsymbol{H}'$ matrix ($H'_{i,i+1} = H'_{i+1,i}$). The wavefunction will also be transformed. The normalization condition of our wavefunction becomes

$$1 = \sum_{j=1}^{N}|\Psi_j|^2\,\xi_j\left(x_{j+(1/2)} - x_{j-(1/2)}\right) = \sum_{j=1}^{N}|\Psi'_j|^2. \tag{3.1.36}$$

For the sake of clarity, in our case for the z and R coordinate $\xi = 1$. For the ρ coordinate we have that $\xi = \rho$. Our wavefunction will be also transformed

$$\Psi'(R, \rho, z) = \Psi(R, \rho, z)\sqrt{\rho\, dR\, dz\, d\rho}. \tag{3.1.37}$$

This method allows the treatment of quantum systems in non-linear and non-cartesian grids avoiding the non-Hermitian discretized Hamiltonian.

3.1.6 Propagation in Imaginary Time

To solve the TDSE we must impose an initial condition, which usually implies imposing an initial wavefunction at the beginning of the pulse. The initial wavefunction is typically the molecular groundstate or a linear combination of states. The obtention of the molecular groundstate is the subject treated in this section.

There are two standard procedures to obtain the eigenstates of a Hamiltonian: the direct diagonalization of the Hamiltonian, derived in section (3.1.5), and the propagation of a wavefunction in imaginary time, which we will discuss here. A general wavefunction can be expanded in a basis of eigenstates of the Hamiltonian. For a time independent Hamiltonian,

$$\Psi\left(\boldsymbol{r}, t\right) = \sum_{n=0}^{\infty} c_n \psi_n\left(\boldsymbol{r}\right) e^{-iE_n t}. \tag{3.1.38}$$

The trick consists on replacing $t \to -i\tau$, so eq. (3.1.38) becomes

$$\Psi\left(\boldsymbol{r}, \tau\right) = \sum_{n=0}^{\infty} c_n \psi_n\left(\boldsymbol{r}\right) e^{-E_n \tau}, \tag{3.1.39}$$

and for a very long τ, the expression will be dominated by the term $n = 0$,

$$\lim_{\tau \to +\infty} \Psi\left(\boldsymbol{r}, \tau\right) = \psi_0\left(\boldsymbol{r}\right) e^{-E_0 \tau}. \tag{3.1.40}$$

To obtain the groundstate we insert at the beginning a trial wavefunction, that should share some general features with the groundstate to ensure a faster convergence. For example, to find the groundstate of the hydrogen atom (an atomic $1s$ orbital) we can place a Gaussian function centred at the nucleus. The propagation is carried out with the previous scheme. For practical reasons, the wavefunction is renormalized every n steps. To ensure convergence we can check the mean value of the energy and verify if it is converged, i.e.

$$\left|E\left[\Psi\left(\boldsymbol{r}, \tau\right)\right] - E\left[\Psi\left(\boldsymbol{r}, \tau + n\Delta t\right)\right]\right| < \varepsilon \tag{3.1.41}$$

for a small ε, where ε is an energy that must be small compared to the energy difference between

two eigenstates. We can also compare the scalar product between the wavefunctions at successive time steps

$$1 - \frac{|\langle \Psi\left(\boldsymbol{r}, \tau\right) | \Psi\left(\boldsymbol{r}, \tau + n\Delta t\right)\rangle|^2}{||\Psi\left(\boldsymbol{r}, \tau\right)||^2 \, ||\Psi\left(\boldsymbol{r}, \tau + n\Delta t\right)||^2} < \delta, \tag{3.1.42}$$

where $\delta \ll 1$.

The excited states can be found iteratively. Having the groundstate wavefunction ψ_0, we can do the following transformation, to remove the contribution of the groundstate

$$\Psi\left(\boldsymbol{r}, \tau = 0\right) = \Phi_{trial}\left(\boldsymbol{r}\right) - \langle \Phi_{trial}|\psi_0\rangle \, \Phi_{trial}\left(\boldsymbol{r}\right) \tag{3.1.43}$$

so $c_0 = 0$, and the propagation will lead to the first excited state. To obtain the ith excited state we must calculate all the previously eigenstates before and apply the transformation

$$\Psi\left(\boldsymbol{r}, \tau = 0\right) = \Phi_{trial}\left(\boldsymbol{r}\right) - \sum_{n=0}^{i-1} \langle \Phi_{trial}|\psi_n\rangle \, \Phi_{trial}\left(\boldsymbol{r}\right) \tag{3.1.44}$$

and then propagate in imaginary time. In principle, you could calculate by this method as many eigenstates as you want, but in practice numerical noise limits that number, since lower eigenstates are reintroduced and they must be removed during the propagation. For states which are very close in energy or even degenerate states, this method does not provide trustable results. However, we can obtain very good results for the groundstate and first excited state of the H_2^+ molecule.

3.1.7 Absorbers

Until now, we have assumed that our wavefunction is fully contained in the numerical grid, assuming that it is sufficiently large to contain all the probability density of the wavefunction. This assumption requires a huge box of hundreds or even thousands of atomic units, since with a laser pulse we can populate continuum states and create a unbound wavepacket that will travel and eventually reach the boundaries, where it will be reflected, producing an artificial effect in the calculation. To avoid this we should calculate in a very large box, but this is unfeasible in most of the situations.

To solve this problem we can absorb the wavefunction near the boundaries of our numerical grid. We have two ways of doing that. The first one is placing an imaginary potential, that will produce a non-Hermitian Hamiltonian, causing a non-conservation of the norm of our wavefunction.

Let us examine in which way the addition of an imaginary potential (also called optical po-
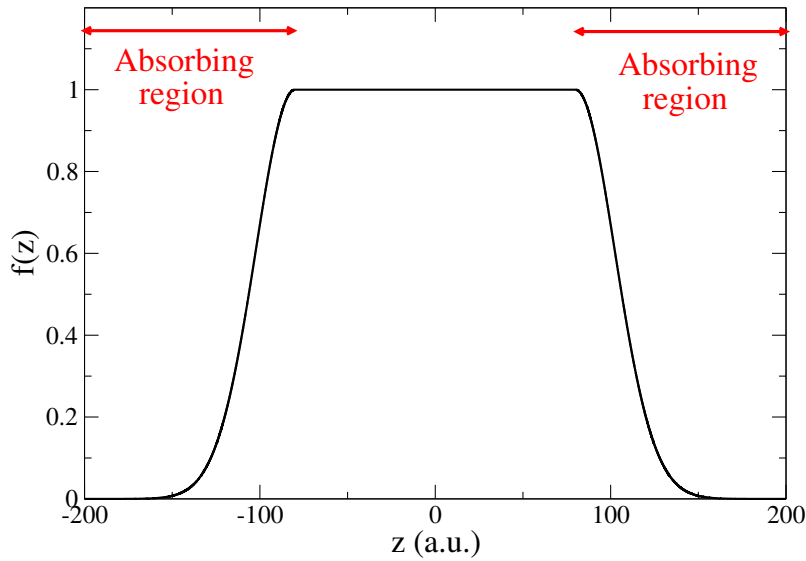
Figure 3.2: Example of a mask function. In this case $z_0 = 80$ a.u. and $\alpha = 0.001$ a.u.

tential) can affect the propagation. If we have our hermitian Hamiltonian $\hat{H}$, and our imaginary potential $-iW(\boldsymbol{r})$, and following a split-operator scheme we will have that

$$\Psi(\boldsymbol{r}, t + \Delta t) = e^{-W(\boldsymbol{r})\frac{\Delta t}{2}} e^{-i\hat{H}\Delta t} e^{-W(\boldsymbol{r})\frac{\Delta t}{2}} \Psi(\boldsymbol{r}, t) \qquad (3.1.45)$$

and here we can see that the probability density is exponentially damped where $W(\boldsymbol{r}) > 0$. In this way we can define an optical potential that is only different from zero near to the boundaries, and we call that region the absorbing region. We will use this kind of absorbing potentials for the calculations in reduced dimensionality models for the H_2^+ molecule, see Chapter 4.

We can also use mask functions. In this method we only multiply our wavefunction by a exponential decaying function, $f(z)$, in the absorbing region. This functions will damp the wavefunction in that region. We will use this kind of approach in the full dimensional calculations for the H_2^+ molecule described in this Chapter. In particular, we will use a mask function of the form

$$f(z) = \begin{cases} 1 & |z| \leq z_0 \\ \exp\left(-\alpha * |z - z_0|^2\right) & z > z_0 \\ \exp\left(-\alpha * |z + z_0|^2\right) & z < -z_0 \end{cases} . \qquad (3.1.46)$$

in each coordinate.

The parameters of these absorbers must be chosen such that they are strong enough to absorb even the fastest parts of the wavefunction, but not too much so that the slowest parts are not

reflected. Besides, their spatial width should be long enough to enclose the particle wavelenght of the slowest parts of the wavefunction.

3.1.8 Virtual Detector Method

The Virtual Detector Method was first introduced by Feuerstein et al [33]. The idea is closely related to the hydrodynamical formulation of the Quantum Mechanics [34]. How can the momentum distribution of the fragments be calculated in an experiment? We can place one detector very far away from the system and calculate the flux through a certain area and at the same time evaluate its momentum. We can then make a histogram and construct the spectrum. The virtual detector is based on the same idea, but now we do not need a physical machine but instead a surface is chosen where the calculation of the flux is done. The absorber is chosen beyond the surface.

We can write the wavefunction as

$$\Psi\left(\boldsymbol{r}, t\right) = A\left(\boldsymbol{r}, t\right) \exp\left(i\phi\left(\boldsymbol{r}, t\right)\right) \tag{3.1.47}$$

where $A\left(\boldsymbol{r}, t\right)$ and $\phi\left(\boldsymbol{r}, t\right)$ are real-valued functions. We know that the flux in quantum mechanics can be derived from the continuity equation. The probability flux is calculated as

$$\boldsymbol{j}\left(\boldsymbol{r}, t\right) = \mathrm{Re}\left(\Psi^*\frac{1}{im}\nabla\Psi\right) \tag{3.1.48}$$

$$= \frac{\left|A\left(\boldsymbol{r}, t\right)\right|^2}{m}\nabla\phi\left(\boldsymbol{r}, t\right). \tag{3.1.49}$$

where m is the mass of the particle. Here we will make a physical assumption. We can think on the probability flux as a local velocity $\boldsymbol{v}\left(\boldsymbol{r}, t\right)$ times a probability density $\left|A\left(\boldsymbol{r}, t\right)\right|^2$. The local momentum can be defined as

$$\boldsymbol{k}\left(\boldsymbol{r}, t\right) = m\boldsymbol{v}\left(\boldsymbol{r}, t\right) = \nabla\phi\left(\boldsymbol{r}, t\right). \tag{3.1.50}$$

so $\boldsymbol{v}\left(\boldsymbol{r}, t\right) = \boldsymbol{j}\left(\boldsymbol{r}, t\right)/\left|A\left(\boldsymbol{r}, t\right)\right|^2$, where $\boldsymbol{j}\left(\boldsymbol{r}, t\right)$ is obtained with (3.1.48).

To obtain the momentum distribution, we define a surface on which we calculate the flux and momentum for each point and time step, and then apply a binning procedure. In our case we will calculate the flux with a five point difference formula, see Appendix A, and then obtain the corresponding momentum. We are assuming that the particle will behave just like a free particle

after crossing the virtual detector. Corrections must be added if the pulse is not over when the particle reaches the detector and if the interaction potential is not negligible.

For the sake of clarity, we will explicitly write the equations for our case. The electron momentum is calculated (in the virtual detector, denoted as $\boldsymbol{r}_d$) as

$$p_z\left(\boldsymbol{r}_d, t\right) = \nabla_z \phi\left(\boldsymbol{r}_d, t\right) - A(t) \tag{3.1.51}$$

$$p_\rho\left(\boldsymbol{r}_d, t\right) = \nabla_\rho \phi\left(\boldsymbol{r}_d, t\right) \tag{3.1.52}$$

where $A\left(t\right)$ is the vector potential. This correction is made if the pulse is not over at the time of measurement, and it is simply the classical change in momentum when an electron is interacting with the field after passing through the virtual detector, see Appendix B. In the ρ direction there is no need of this correction, since the field is polarized in the z direction. The electronic energy is then

$$E_{elec} = \frac{p_z^2}{2} + \frac{p_\rho^2}{2} + V_{eN}. \tag{3.1.53}$$

In the limit, $V_{eN} \to 0$ for $z, \rho \to \infty$.

After ionization the nuclei will evolve along the Coulomb explosion curve. Since this curve is always dissociative, the nuclear momentum can be computed. We will have then a nuclear momentum distribution. When the electron is detected in the virtual detector the nuclei have had not time to dissociate, the interaction potential between the nuclei can not be neglected. We can calculate the nuclear momentum at the virtual detector, compute the kinetic energy associated and then sum the interaction potential to account for this extra kinetic energy. The nuclear energy will be computed as

$$E_N = \frac{\nabla_R \phi\left(\boldsymbol{r}_d, t\right)^2}{2\mu} + \frac{1}{R} \tag{3.1.54}$$

and the nuclear momentum in the asymptotic region as

$$P_N = \sqrt{2\mu E_N} \tag{3.1.55}$$

where μ is the reduced mass of the nuclei. This method allows to calculate of photoelectron spectra and nuclear kinetic energy spectra.
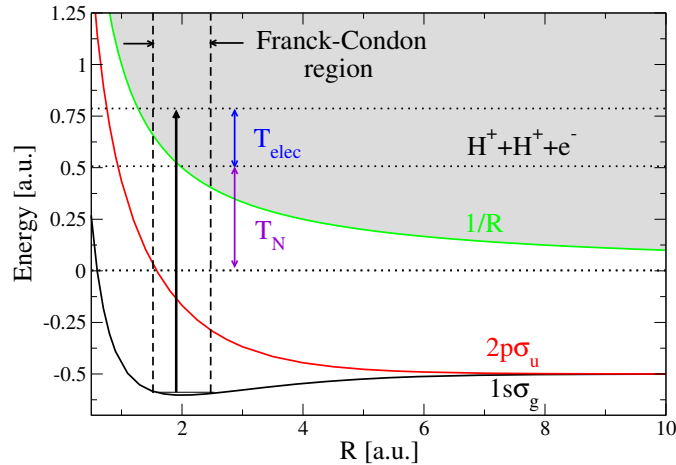
Figure 3.1: The Born-Oppenheimer curves calculated in a 3D calculation. The black arrow represents a vertical transition from the H_2^+ groundstate to the ionization channel with a energy photon enough to directly ionize the molecule. The dashed lines represents the limits of the Franck-Condon region.

3.2 Results for direct ionization

We have preliminary results that show that the Virtual Detector Method can extract accurate EKE and PKE spectra in H_2^+ photoionization. Our three–dimensional grid spans a total of 30 a.u. in R-direction and 100 a.u.$\times$50 a.u. in the $z \times \rho$ plane with a minimum grid spacing of $\Delta R = 0.05$ a.u. and $\Delta \rho = \Delta z = 0.1$ a.u. These grid spacings gradually increase towards the outer grid boundaries. The time step for the electronic propagation is $\Delta t_{elec} = 0.015$ a.u. and for the nuclear propagation, $k = 10$.

We have performed a scan in the energy of the photon, ω, and in the length of the pulse. The envelope of our pulse has a sin-square shape with a peak intensity of 10^{13} W/cm^2. All the photon energies used will be enough to induce the photoionization of the H_2^+ molecule at the Franck-Condon region. The analysis of the momentum and energy of the fragments was done using the virtual detector method. We show the results in figs. 3.2, 3.3, 3.4, and 3.5.

The photoelectron spectrum is shown in fig. 3.2 for different photon energies. The position of the central peak changes accordingly to the photon energy. We have choosen $R = 2.22$ a.u. to calculate the nuclear energy. In fig. 3.3 we see that the maximum probability corresponds to a nuclear energy of $E_N = 0.45$ a.u., which corresponds to an internuclear distance $R \sim 2.22$ a.u. (since $E_N = 1/R$). In the same figure, there appears a second peak for slower protons that disappears when the photon energy increases. The reason for this is that there is a minimum
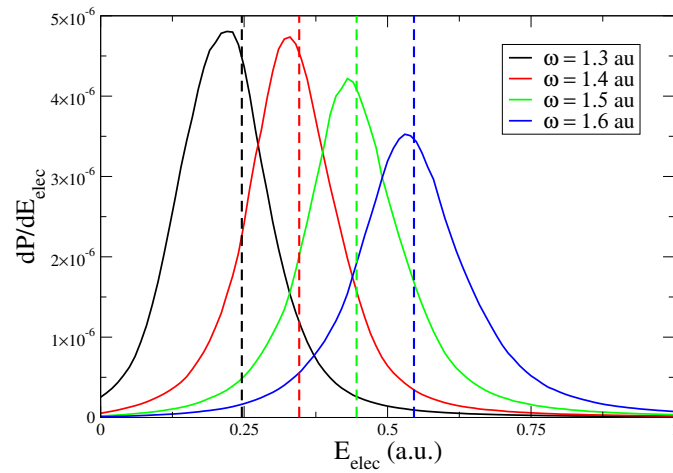
Figure 3.2: Photoelectron spectrum for different photon energies. The dashed lines are the expected central position for the spectrum calculated with $R = 2.22\,a.u.$, and are calculated as $\omega - IP - V_{NN}(R = 2.22\,a.u.)$. The pulse duration is FWHM= 1 fs in all cases.
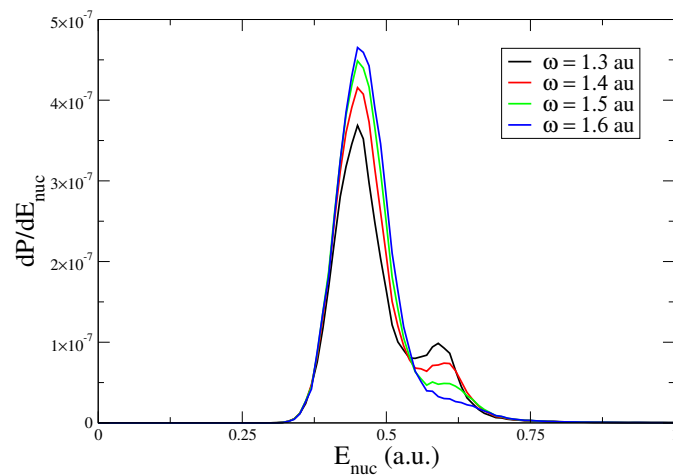
Figure 3.3: Nuclear energy spectrum for different photon energies with FHWM = 0.2 fs. The peak is located at 0.45 a.u., which corresponds to $R = 2.22$ a.u.
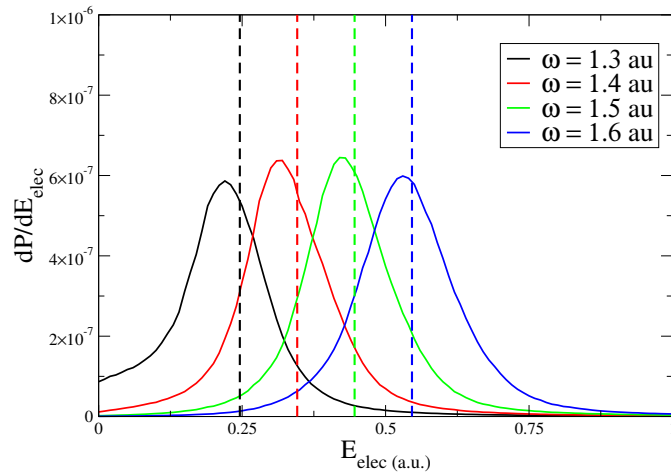
Figure 3.4: Same as in fig. 3.2 for FWHM= 0.5 fs.
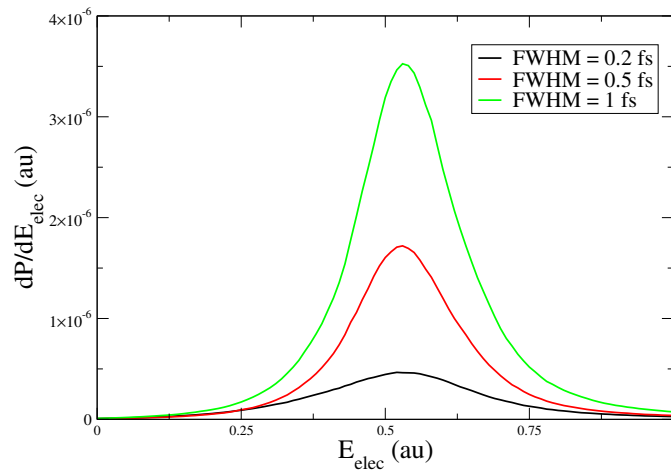
Figure 3.5: Photoelectron spectrum for different FWHM. All the calculations have $\omega = 1.6$ a.u.

in the ionization probability around $R \sim 2$ a.u., which moves to smaller values of R (outside of the Franck-Condon region) as the photon energy increases (see e.g. [35] and fig. 4.4 of this Master Thesis, obtained in the Fixed Nuclei Approximation). The same photoelectron spectra for FWHM= 0.5 fs and the same pulse duration are shown in fig. 3.4. Results are similar, although the distributions are wider as expected, since the energy width of the pulse is wider. In fig. 3.5 we can see this dependence. Larger pulses correspond to shorter bandwidths in the photoelectron spectrum. The absolute value is larger for the long pulse since the pulse it has more time to ionize the molecule.

These results show the validity of the method. We can obtain accurate kinetic energy spectra both in electron and nuclear energy. With this method, we intend to obtain accurate PKE and

EKE for a variety of photoionization and dissociation processes, as well as angular distributions (which can be directly obtained from the electron momenta). In particular, we will focus in non-adiabatic and multiphoton absorption processes, for which close-coupling methods and BO-based methods are not feasible.

Chapter 4

Resolvent Technique applied to molecules

"The most exciting phrase to hear in science, the one that heralds new discoveries, is not 'Eureka!', but 'That's funny ...'."

Isaac Asimov

4.1 Theory

In this Chapter, we present an alternative method, to that presented in Chapter 3, for extracting observables from a grid calculation. We will present an extension for molecules of a technique used to obtain the photoelecton spectra in atoms, the Resolvent Technique.

4.1.1 Resolvent Technique in Atoms

The Resolvent Technique is useful to extract the energy spectrum at the end of the laser pulse, and it requires that all the wavefunction is contained in the grid. It was first introduced by Kulander et. al [36]. The first calculations based on this technique were compared with experiments in arbitrary units [37–39]. Only more than twenty years late the proportionality constant was described, making this technique able to calculate the probability density [11]. We will show the theory that already existed, which can be applied to study atomic photoionization.

The idea beyond this method is to use an operator to select only states which lie in a particular energy range. We can start by assuming that the wavefunction at the end of the pulse is a sum over bound states and an integral over continuum states, all of them eigenstates of the field-free

Hamiltonian. The bound states are normalized to unity, and the continuum states normalized to the Dirac's delta function. In the following, $|b\rangle$ represents bound states and $|\varepsilon\rangle$ represents continuum states. For the sake of simplicity, we will drop the indexes for other quantum numbers. Therefore

$$|\Psi\rangle = \sum_b c_b |b\rangle + \int d\varepsilon c(\varepsilon) |\varepsilon\rangle. \tag{4.1.1}$$

Denoting the field free Hamiltonian as $\hat{H}_0$, we will have the following relationships for the $|b\rangle$ and $|\varepsilon\rangle$ states:

$$\hat{H}_0 |b\rangle = E_b |b\rangle \tag{4.1.2}$$
$$\hat{H}_0 |\varepsilon\rangle = \varepsilon |\varepsilon\rangle \tag{4.1.3}$$
$$\langle\varepsilon|\varepsilon'\rangle = \delta(\varepsilon - \varepsilon') \tag{4.1.4}$$
$$\langle b|b'\rangle = \delta_{b,b'} \tag{4.1.5}$$
$$\langle\varepsilon|b\rangle = 0. \tag{4.1.6}$$

The normalization condition of the wavefunction will be

$$1 = \sum_b |c_b|^2 + \int dE \rho(E), \tag{4.1.7}$$

where we define a probability density $\rho(E) = |c(E)|^2$ for the continuum states. In both cases, the eigenvalue of the Hamiltonian represents the total energy of the system. In the case of a one-electron atom we can directly link this energy to the photoelectron energy.

Since we are in a grid method, we do not have a explicit knowledge of the eigenstates. We can start by defining the resolvent operator as

$$\hat{R}_\delta^n(E) = \frac{\delta^n}{\left(E - \hat{H}_0\right)^n - i\delta^n} \tag{4.1.8}$$

and its adjoint is

$$\hat{R}_\delta^n(E)^\dagger = \frac{\delta^n}{\left(E - \hat{H}_0\right)^n + i\delta^n}, \tag{4.1.9}$$

where n is the order of the resolvent operator, δ its resolution and E is the selected energy.

We can write the resolvent operator as a product of Green operators,

$$\hat{R}_\delta^n(E) = \frac{\delta^n}{\left(E - \hat{H}_0\right)^n - i\delta^n} \equiv \prod_{j=1}^{n} \delta G\left(E - q_j\delta\right), \qquad (4.1.10)$$

where

$$G\left(E - q_j\delta\right) = \frac{1}{E - q_j\delta - \hat{H}_0} \qquad (4.1.11)$$

and $q_j = i^{1/n}z_j$, where $z_j = e^{i2\pi\frac{j-1}{n}}$ is the jth complex root of the unity. This is an important simplification in the computational implementation of the method, since it allows to treat it as an inversion problem. We can define $|\Psi'\rangle \equiv \hat{R}_\delta^n(E)|\Psi\rangle$, which is the result of applying the resolvent operator to a general state. The modulus square of $|\Psi'\rangle$ is proportional to the probability density. We will now prove the previous statement and find the proportional constant:

$$\langle\Psi'|\Psi'\rangle = \langle\Psi|\hat{R}_\delta^n(E)^\dagger \hat{R}_\delta^n(E)|\Psi\rangle = \left\langle\Psi\left|\frac{\delta^{2n}}{\left(E - \hat{H}_0\right)^{2n} + \delta^{2n}}\right|\Psi\right\rangle \qquad (4.1.12)$$

$$= \sum_b |c_b|^2 K\left(E - E_b, \delta, n\right) + \int d\varepsilon\, |c(\varepsilon)|^2 K\left(E - \varepsilon, \delta, n\right) \qquad (4.1.13)$$

$$\equiv P\left(E, \delta, n\right), \qquad (4.1.14)$$

where we have defined the quantity $K\left(E, \delta, n\right) = \frac{\delta^{2n}}{E^{2n} + \delta^{2n}}$. This function has always a maximum at $E = 0$, where $K\left(0, \delta, n\right) = 1$, see fig. 4.1. At $E = \pm\delta$, $K\left(\pm\delta, \delta, n\right) = 0.5$. At $\pm\infty$ it goes to zero. Its most interesting feature is that this function is very similar to the boxcar function $\Pi_{a,b}(E)$, a function that is 1 in the interval $[a, b]$ and zero elsewhere, being $a = -\delta$ and $b = \delta$. In fact, $\lim_{n\to\infty} K\left(E, \delta, n\right) = \Pi_{-\delta,\delta}(E)$.

Taking into account the properties of $K\left(E, \delta, n\right)$ we can conclude that the quantity $\langle\Psi'|\Psi'\rangle$ is dominated by the states that are close to the energy that appears in the resolvent operator. Only energies in the interval $[E - \delta, E + \delta]$ have a significant weight in the sum. For any energy close to a bound energy $\langle\Psi'|\Psi'\rangle \propto |c_b|^2$, and for any energy in the continuum, $\langle\Psi'|\Psi'\rangle \propto |c(E)|^2 = \rho(E)$. The problem now relies on the obtention of the constant that relates this quantity to the real probability density [11]. We can suppose without loss of generality that the continuum states are all states with $E > 0$. If we take a positive energy in the resolvent operator, the contribution of the sum over bound states will be negligible. In this way eq. 4.1.13 can be approximated by
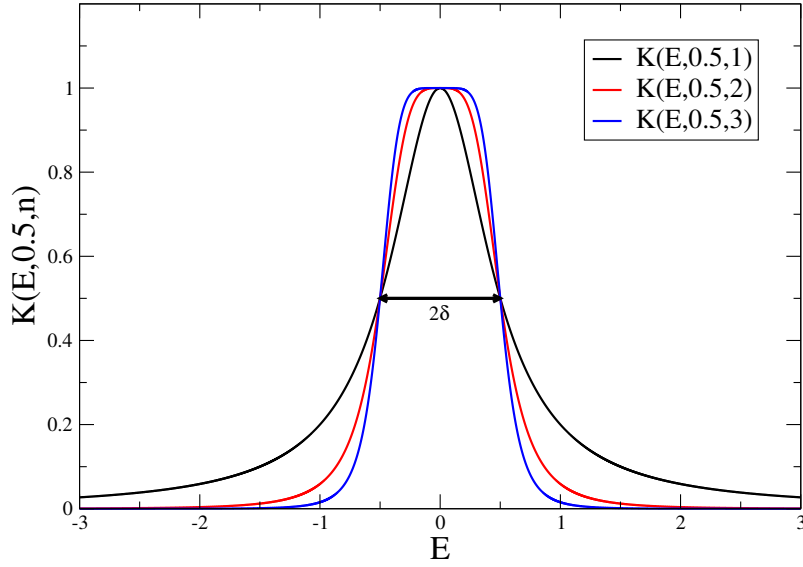
Figure 4.1: Plot of $K(E, 0.5, n)$ for different values of n.

$$P(E, \delta, n) \approx \int_{\varepsilon > 0} d\varepsilon \, |c(\varepsilon)|^2 \, K(E - \varepsilon, \delta, n) \tag{4.1.15}$$

$$\approx |c(E)|^2 \int_{\varepsilon > 0} d\varepsilon K(E - \varepsilon, \delta, n) \tag{4.1.16}$$

$$\approx |c(E)|^2 \int_{-\infty}^{\infty} d\varepsilon K(E - \varepsilon, \delta, n) \tag{4.1.17}$$

The first approximation neglects the sum over the bound states for a positive energy. The second approximation is reasonable in the sense that if δ is small enough, $|c(E)|^2$ has the same value in the interval $[E - \delta, E + \delta]$ and it can be subtracted from the integral. The last approximation is based on the fact that the integral in a region far from E is negligible. The proportional constant that relates $P(E, \delta, n)$ with the probability $|c(E)|^2$ is thus

$$\int_{-\infty}^{\infty} d\varepsilon K(E - \varepsilon, \delta, n) = \frac{\pi}{n} \delta \csc\left(\frac{\pi}{2n}\right) \tag{4.1.18}$$

This integral $\lim_{n \to \infty} \int_{-\infty}^{\infty} d\varepsilon K(E - \varepsilon, \delta, n) = \int_{-\infty}^{\infty} \Pi_{-\delta, \delta}(E - \varepsilon) d\varepsilon = 2\delta$ as expected. Therefore,

$$\rho(E) = \frac{P(E, \delta, n)}{\frac{\pi}{n} \delta \csc\left(\frac{\pi}{2n}\right)} \tag{4.1.19}$$

A similar treatment can be applied to bound states. In this case only the integration $\int_{E_b - \delta}^{E_b + \delta} d\varepsilon \rho(\varepsilon) \approx$

$|c_b|^2$ is meaningful, since the integral provides an approximation to the probability of that bound state.

In the calculations we will not have a real continuum, since all calculations are performed in a finite box and all states are discretized. In this way, the choice of δ must obey to some considerations. If it is too small, it will show the peaks that correspond to the discretization of the box. If it is too large, we will lose resolution in the spectrum and features like ATI peaks will be lost. So a criterion can be that the interval δ of energy must contain one discretized state. This means that the density of states, ρ_{st}, multiplied by δ, should be approximately one ($\rho_{st}\delta \approx 1$).

This technique can be a very useful tool to study and calculate the photoelectron spectrum. On the other hand, one of the drawbacks of this method is that it is only applicable when we have only one fragment to analyse. We will show in this work that we can study also molecular systems (ionization and dissociation) with minor alterations in the method.

4.1.2 Resolvent Technique in Molecules

The Resolvent Technique described before for atoms can be extended to molecules, within the Born-Oppenheimer approximation. This approximation is based on two things: we assume that a stationary wavefunction of the molecular Hamiltonian is of the form

$$\Psi_i^\nu \left(\mathbf{r}, \mathbf{R} \right) = \Phi_i \left(\mathbf{r}; \mathbf{R} \right) \chi_i^\nu \left(\mathbf{R} \right), \tag{4.1.20}$$

where the electronic wavefunction depends parametrically on the nuclear coordinate,

$$\hat{H}_{el} \Phi_i \left(\mathbf{r}; \mathbf{R} \right) = E_i \left(\mathbf{R} \right) \Phi_i \left(\mathbf{r}; \mathbf{R} \right), \tag{4.1.21}$$

$$\left[\hat{T}_N + E_i \left(\mathbf{R} \right) \right] \chi_i^\nu \left(\mathbf{R} \right) = W_i^\nu \chi_i^\nu \left(\mathbf{R} \right). \tag{4.1.22}$$

The latter two equations are respectively the electronic and nuclear Schrödinger equations. The molecular Hamiltonian is the sum over the nuclear kinetic energy operator and the electronic Hamiltonian, $\hat{H} = \hat{H}_{el} + \hat{T}_N$. Using 4.1.20

$$\hat{H}\Psi_i^\nu\left(\mathbf{r},\mathbf{R}\right) \;=\; \left[\hat{H}_{el}+\hat{T}_N\right]\Psi_i^\nu\left(\mathbf{r},\mathbf{R}\right) \tag{4.1.23}$$

$$=\; \left[\hat{H}_{el}\Phi_i\left(\mathbf{r};\mathbf{R}\right)\chi_i^\nu\left(\mathbf{R}\right)+\hat{T}_N\Phi_i\left(\mathbf{r};\mathbf{R}\right)\chi_i^\nu\left(\mathbf{R}\right)\right] \tag{4.1.24}$$

$$=\; \left[E_i\left(\mathbf{R}\right)\Phi_i\left(\mathbf{r};\mathbf{R}\right)\chi_i^\nu\left(\mathbf{R}\right)+\hat{T}_N\Phi_i\left(\mathbf{r};\mathbf{R}\right)\chi_i^\nu\left(\mathbf{R}\right)\right] \tag{4.1.25}$$

This ansatz is only a molecular eigenstate if $\hat{T}_N\Phi_i\left(\mathbf{r};\mathbf{R}\right)\chi_i^\nu\left(\mathbf{R}\right)\approx\Phi\left(\mathbf{r};\mathbf{R}\right)\hat{T}_N\chi_i^\nu\left(\mathbf{R}\right)$. This means that the BO approximation is valid when the electronic wavefunction depends very smoothly on the nuclear coordinates.

We can define the resolvent operator in the BO approximation,

$$\hat{R}\left(E_N,\varepsilon_{ele},\alpha_0,\delta_N,\delta_e,n_N,n_e\right) \;=\; \frac{\delta_N^{n_N}}{\left[\left(\hat{T}_N+E_{\alpha_0}\left(R\right)+\varepsilon_{ele}\right)-E_N-E_{\alpha_0}\left(\infty\right)-\varepsilon_{ele}\right]^{n_N}-i\delta_N^{n_N}}$$
$$\times\frac{\delta_e^{n_e}}{\left[\hat{H}_{el}-E_{\alpha_0}\left(R\right)-\varepsilon_{ele}\right]^{n_e}-i\delta_e^{n_e}} \tag{4.1.26}$$

where E_N and ε_{ele} are the nuclear and electronic energy selected, respectively, α_0 is the electronic curve selected, δ_N and δ_e are the resolution , and n_N and n_e are the order of the resolvent operator for nuclear and electronic energy, respectively. The resolvent operator is then the product of a nuclear resolvent $(\hat{R}_N)$ and an electronic resolvent $(\hat{R}_{ele})$.

The idea is the following: first, an the electronic curve α_0 is selected with a given electronic energy, and then the proper vibrational state is chosen. If α_0 is a electronic bound curve, we will take $\varepsilon_{ele}=0$, and if it is a continuum state (like the $1/R$ Coulomb explosion curve) we take $\varepsilon_{ele}\geq 0$. For $\varepsilon_{ele}\geq 0$ we will obtain copies of the electronic curves by summing the energy of the electron that is in the continuum.

The operator (4.1.26) selects first one particular electronic state, and then it resolves the vibronic energy. In the expansion of a general wavefunction as a sum of Born-Oppenheimer states:

$$
\begin{aligned}
|\Psi\rangle \;=\;& \sum_{\alpha=bound} |\,\Phi_\alpha\,(R)\rangle \left\{ \sum_\nu c_\alpha^\nu \,|\, \chi_\alpha^\nu\rangle + \int_{W_\alpha > E_\alpha(\infty)} dW_\alpha c_\alpha\,(W_\alpha)\,|\, \chi_\alpha^{W_\alpha}\rangle \right\} \\
&+ \sum_{\alpha=continuum} \int_{\varepsilon>0} d\varepsilon \,|\,\Phi_{\alpha,\varepsilon}\,(R)\rangle \\
&\times \left\{ \sum_\nu c_\alpha^\nu\,(\varepsilon)\,|\,\chi_{\alpha,\varepsilon}^\nu\rangle + \int_{W_{\alpha,\varepsilon} > E_{\alpha,\varepsilon}(\infty)} dW_{\alpha,\varepsilon} c_\alpha\,(\varepsilon, W_{\alpha,\varepsilon})\,|\,\chi_{\alpha,\varepsilon}^{W_{\alpha,\varepsilon}}\rangle \right\} \qquad (4.1.27) \\
\equiv\;& |b,b\rangle + |b,c\rangle + |c,b\rangle + |c,c\rangle \qquad\qquad\qquad\qquad\qquad\qquad\quad (4.1.28)
\end{aligned}
$$

Four different terms are present: states that are electronically unbound and vibrationally bound, which will be denoted by $|c,b\rangle$, and states that are both electronically and vibrationally bound, $|b,b\rangle$ and $|c,c\rangle$ and $|b,c\rangle$ states, defined analogously. Note that, for example, non-dissociative ionization is included in $|c,b\rangle$ states.

In H_2^+ there are no bound electronic curves in the continuum, only the dissociative Coulomb explosion curve. For this reason, here we will ignore the $|c,b\rangle$ states.

From now on we will apply the BO approximation. As in the previous section, the physically interesting quantity is $\langle \Psi | \hat{R}^\dagger \hat{R} | \Psi \rangle$. We will calculate $\hat{R}\,|\Psi\rangle$ by parts. We will start by $\hat{R}\,|b,b\rangle$, where $\varepsilon_{ele} = 0$:

$$
\begin{aligned}
\hat{R}\,|b,b\rangle \;=\;& \sum_\nu \frac{\delta_N^{n_N}}{\left[\left(\hat{T}_N + E_{\alpha_0}(R)\right) - E_N - E_{\alpha_0}(\infty)\right]^{n_N} - i\delta_N^{n_N}} \qquad (4.1.29) \\
&\times \frac{\delta_e^{n_e} c_{\alpha_0}^\nu \,|\Phi_{\alpha_0}(R)\rangle \,|\chi_{\alpha_0}^\nu(R)\rangle}{\left[E_{\alpha_0}(R) - E_{\alpha_0}(R)\right]^{n_e} - i\delta_e^{n_e}} \\
&+ \sum_{\alpha \neq \alpha_0,\nu} \hat{R}_N \frac{\delta_e^{n_e} c_{\alpha_0}^\nu \,|\Phi_{\alpha_0}(R)\rangle \,|\chi_\alpha^\nu(R)\rangle}{\left[E_\alpha(R) - E_{\alpha_0}(R)\right]^{n_e} - i\delta_e^{n_e}}
\end{aligned}
$$

One reasonable simplification is to neglect the second term, since for $\alpha \neq \alpha_0$ and if $\delta_e \ll E_\alpha(R) - E_{\alpha_0}(R)$ we know from the previous section that we can neglect that contribution to the resolvent operator. We obtain

$$
\hat{R}\,|b,b\rangle = \sum_\nu \frac{\delta_N^{n_N}}{\left[(W_{\alpha_0}^\nu) - E_N - E_{\alpha_0}(\infty)\right]^{n_N} - i\delta_N^{n_N}} \frac{c_{\alpha_0}^\nu \,|\Phi_{\alpha_0}(R)\rangle \,|\chi_{\alpha_0}^\nu(R)\rangle}{-i} \qquad (4.1.30)
$$

where $W_{\alpha_0}^\nu$ is the vibronic (nuclear plus electronic) energy. Proceeding in the same way for $\hat{R}\,|b,c\rangle$ we obtain

$$\hat{R}\left|b,c\right\rangle = \int_{W_{\alpha_0}>E_{\alpha_0}(\infty)} dW_{\alpha_0} \frac{\delta_N^{n_N}}{\left[(W_{\alpha_0})-E_N-E_{\alpha_0}(\infty)\right]^{n_N}-i\delta_N^{n_N}} \tag{4.1.31}$$
$$\times \frac{c_{\alpha_0}(W_{\alpha_0})\left|\Phi_{\alpha_0}(R)\right\rangle\left|\chi_{\alpha_0}^{\nu}(R)\right\rangle}{-i}$$

For calculating $\hat{R}\left|c,c\right\rangle$, the sum over electronic curves that are not included in the resolvent operator can be neglected. For that reason, we will drop the index for the electronic curve:

$$\hat{R}\left|c,c\right\rangle = \int d\varepsilon \int_{W_\varepsilon>\varepsilon+E(\infty)} dW_\varepsilon \hat{R}_N \hat{R}_{ele} c\left(\varepsilon,W_\varepsilon\right)\left|\Phi_\varepsilon(R)\right\rangle\left|\chi_\varepsilon^{W_\varepsilon}\right\rangle \tag{4.1.32}$$
$$= \int d\varepsilon \int_{W_\varepsilon>\varepsilon+E(\infty)} dW_\varepsilon \frac{\delta_N^{n_N}}{\left[\left(\hat{T}_N+E(R)+\varepsilon_{ele}\right)-E_N-E(\infty)-\varepsilon_{ele}\right]^{n_N}-i\delta_N^{n_N}}$$
$$\times \frac{\delta_e^{n_e}}{\left[\hat{H}_{el}-E(R)-\varepsilon_{ele}\right]^{n_e}-i\delta_e^{n_e}} c\left(\varepsilon,W_\varepsilon\right)\left|\Phi_\varepsilon(R)\right\rangle\left|\chi_\varepsilon^{W_\varepsilon}\right\rangle$$
$$= \int d\varepsilon \int_{W_\varepsilon>\varepsilon+E(\infty)} dW_\varepsilon \frac{\delta_N^{n_N}}{\left[W_\varepsilon-E_N-E(\infty)-\varepsilon_{ele}\right]^{n_N}-i\delta_N^{n_N}}$$
$$\times \frac{\delta_e^{n_e}}{\left[\varepsilon-\varepsilon_{ele}\right]^{n_e}-i\delta_e^{n_e}} c\left(\varepsilon,W_\varepsilon\right)\left|\Phi_\varepsilon(R)\right\rangle\left|\chi_\varepsilon^{W_\varepsilon}\right\rangle$$

Note that the vibronic energy is the sum of the nuclear energy and the electronic energy,

$$W_{\alpha_0,\varepsilon_{ele}} = \varepsilon_{ele}+E_N+E_{\alpha_0}(\infty). \tag{4.1.33}$$

The next step is the calculation of $\langle\Psi|\hat{R}^\dagger\hat{R}|\Psi\rangle$. Since all Born-Oppenheimer states are orthogonal to each other we will have that

$$\langle\Psi|\hat{R}^\dagger\hat{R}|\Psi\rangle = \langle b,b|\hat{R}^\dagger\hat{R}|b,b\rangle + \langle b,c|\hat{R}^\dagger\hat{R}|b,c\rangle + \langle c,c|\hat{R}^\dagger\hat{R}|c,c\rangle \tag{4.1.34}$$

The first two terms in the sum can be treated exactly as in the Resolvent Technique for atoms. The differential probability in the nuclear energy for a bound electronic curve, $\frac{dP^{\alpha_0}}{dE_N}$, is only affected by a constant,

$$\frac{dP^{\alpha_0}}{dE_N} = \langle\Psi|\hat{R}^\dagger\hat{R}|\Psi\rangle \frac{1}{\frac{\pi}{n_N}\delta_N\csc\left(\frac{\pi}{2n_N}\right)}. \tag{4.1.35}$$

In this way, we will be able to calculate the differential probability of the nuclear energy for

each electronic curve. In the third term, equation (4.1.34), we must find the relationship between $|c\left(\varepsilon_{elec}, W_{\varepsilon_{elec}}\right)|^2$ and $\langle c, c|\hat{R}^\dagger \hat{R}|c, c\rangle$,

$$
\begin{aligned}
\langle c, c|\hat{R}^\dagger \hat{R}|c, c\rangle &= \int d\varepsilon \int_{W_\varepsilon > \varepsilon + E(\infty)} dW_\varepsilon K\left(W_\varepsilon - W_{\varepsilon_{ele}}, \delta_N, n_N\right) \\
&\quad \times K\left(\varepsilon - \varepsilon_{ele}, \delta_e, n_e\right)|c\left(\varepsilon, W_\varepsilon\right)|^2 \\
&\approx |c\left(\varepsilon_{ele}, W_{\varepsilon_{ele}}\right)|^2 \int d\varepsilon \int_{W_\varepsilon > \varepsilon + E(\infty)} dW_\varepsilon \\
&\quad \times K\left(W_\varepsilon - W_{\varepsilon_{ele}}, \delta_N, n_N\right) K\left(\varepsilon - \varepsilon_{ele}, \delta_e, n_e\right) \\
&\approx |c\left(\varepsilon_{ele}, W_{\varepsilon_{ele}}\right)|^2 \int_{-\infty}^{+\infty} d\varepsilon \int_{-\infty}^{+\infty} dW_\varepsilon \\
&\quad \times K\left(W_\varepsilon - W_{\varepsilon_{ele}}, \delta_N, n_N\right) K\left(\varepsilon - \varepsilon_{ele}, \delta_e, n_e\right) \\
&= |c\left(\varepsilon_{ele}, W_{\varepsilon_{ele}}\right)|^2 \frac{1}{\frac{\pi}{n_N}\delta_N \csc\left(\frac{\pi}{2n_N}\right)} \frac{1}{\frac{\pi}{n_e}\delta_e \csc\left(\frac{\pi}{2n_e}\right)}.
\end{aligned}
$$

$$(4.1.36)$$
$$(4.1.37)$$
$$(4.1.38)$$
$$(4.1.39)$$

Here $|c\left(\varepsilon_{ele}, W_{\varepsilon_{ele}}\right)|^2$ is the double differential probability, for a particular electronic curve in the electronic and vibronic energy. Using eq. (4.1.33), we conclude that

$$
\frac{d^2 P^{\alpha_0}}{dW_{\varepsilon_{ele}} d\varepsilon_{ele}} = \frac{d^2 P^{\alpha_0}}{dE_N d\varepsilon_{ele}}, \tag{4.1.40}
$$

therefore

$$
\frac{d^2 P^{\alpha_0}}{dE_N d\varepsilon_{ele}} = \langle \Psi|\hat{R}^\dagger \hat{R}|\Psi\rangle \frac{1}{\frac{\pi}{n_N}\delta_N \csc\left(\frac{\pi}{2n_N}\right)} \frac{1}{\frac{\pi}{n_e}\delta_e \csc\left(\frac{\pi}{2n_e}\right)}. \tag{4.1.41}
$$

The previous formula will allow us to calculate the differential probability in coincidence of the nuclear energy and the electronic energy by selecting a particular electronic curve.

In conclusion, we have derived a formal way to obtain the doubly differential probability and the proton kinetic energy spectrum from different channels. To evaluate the validity of the method we have performed several calculations that are shown in the next section.

4.2 Results

We have performed calculations to validate the method described in the previous section. We work on a reduced dimensionality model of the H_2^+ molecule, with one degree of freedom for
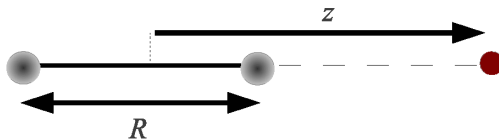
Figure 4.1: Coordinate system used to describe the H_2^+ system in a reduced dimensionality model.

the electron and one for the nuclear motion (usually noted as 1+1D). The propagation of the wavefunction is described in [40]. The pulse is assumed to have linear polarization along the molecular axis. We also use an improved soft-core potential described in [40] to describe in a more realistic way the real molecule in a reduced dimensionality model. The analysis is done with the Resolvent Technique for molecules. The shape of the pulse will be modelled always by a sin-square envelope. We will use Ω to indicate the photon energy for each case. The grid size is $z \in [-1500, 1500]$a.u., $R \in [0, 30]$a.u., with $dz = 0.1$ a.u., $dR = 0.05$ a.u. and $dt = 0.02$ a.u. .

4.2.1 One-photon absorption

We use an XUV pulse with a photon energy of $\Omega = 1.37$ a.u. and a total duration of 16 fs (144 optical cycles) to ionize directly our molecule via one-photon transition. The peak intensity of the pulse is 10^{14} W/cm^2. The Born-Oppenheimer curves of H_2^+ are shown in fig. 4.2.

We present the doubly differential probability for the Coulomb explosion in fig. 4.3 as a function of electronic energy and nuclear energy, both in linear (left) and in logarithmic (right) scales. In this figure, information about the photoionization of the H_2^+ molecule can be obtained, in particular on how the energy is shared between the electron and nuclei. Since the total energy must be conserved, the distribution should be on a line with slope -1. In both plots we see such line, which corresponds to the absorption of one XUV photon. In the log plot the line corresponding to two-photon absorption is also visible. Both lines are parallel, and the energy separation between them is Ω as expected.

One interesting feature can be observed at nuclear energy around 0.5 a.u., where there is a probability depletion. This nuclear energy corresponds to being at $R = 2$ a.u. in the Coulomb explosion curve (since $T_N \sim 1/R$). To check the origin of such feature we have performed a calculation of the ionization probability, in the Fixed-Nuclei Approximation, for each value of R with the same pulse. This result is plotted in fig. 4.4. There is a minimum at $R = 2$ a.u. that explains the depletion of the probability in the fig. 4.3. This effect was already observed in [35].
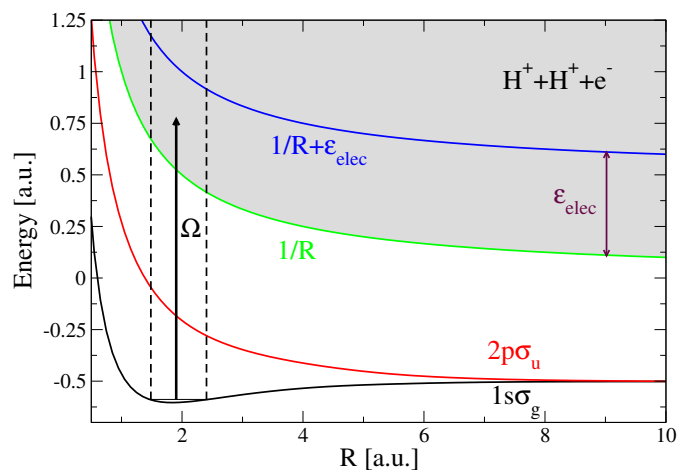
Figure 4.2: Born-Oppenheimer potential energy curves calculated in a 1D model. The black arrow represents a vertical transition from the H_2^+ groundstate to the ionization channel with a photon energy $\Omega = 1.37$ a.u.. The dashed lines represent the limits of the Franck-Condon region.
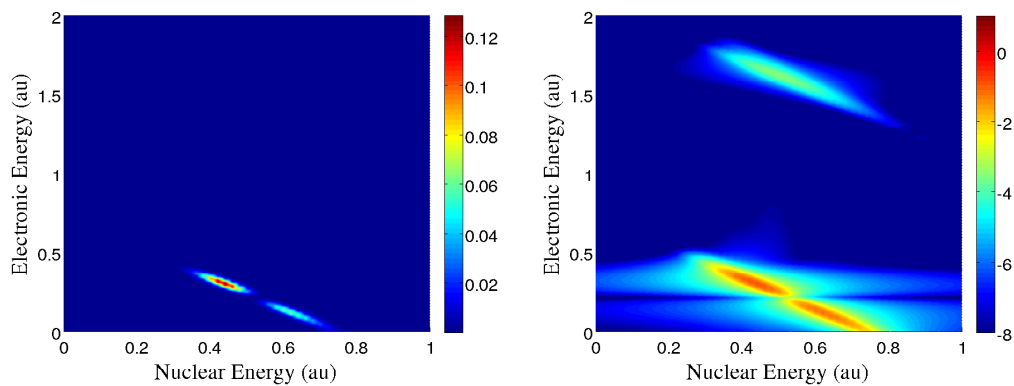
Figure 4.3: Doubly differential probability for $\Omega = 1.37$ a.u., in linear (left) and logarithmic (right) scale. The distribution lies on lines with slope -1.
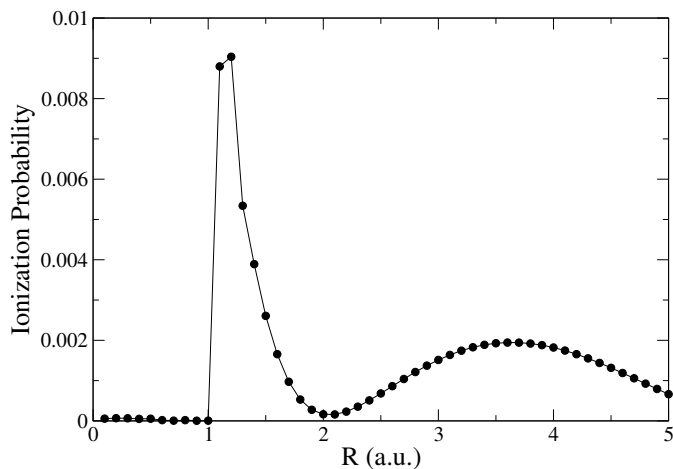
Figure 4.4: Ionization probability as a function of the internuclear distance R.
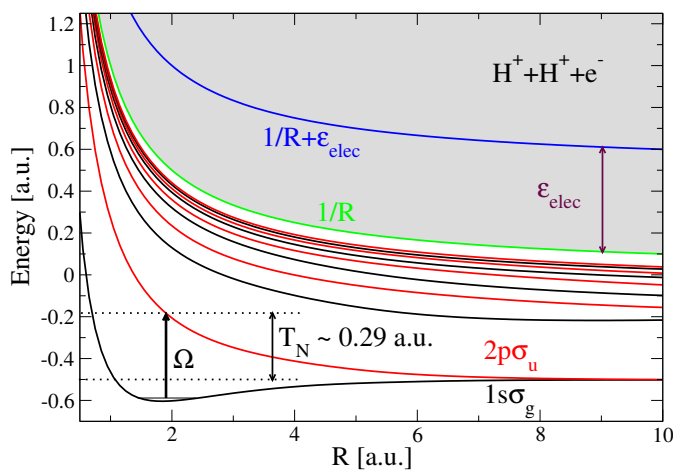
Figure 4.5: Same as fig. (4.2) for $\Omega = 0.398$ a.u. . The black curves represent states with gerade parity and the red curves represent states with ungerade parity.

4.2.2 Resonant transition $1s\sigma_g \to 2p\sigma_u$

To validate the extraction of the nuclear energy spectrum for a specific electronic curve, we have chosen a pulse with the same duration and intensity that in the previous case but changing the photon energy to one capable of inducing a resonant transition between the $1s\sigma_g$ and $2p\sigma_u$ states at the equilibrium internuclear distance. The photon energy for this case is $\Omega = 0.398$ a.u. (7th harmonic of an 800 nm IR photon) . The Born-Oppenheimer curves are shown in fig. 4.5. We expect to have a huge contribution of the $2p\sigma_u$ channel to the proton kinetic energy spectrum. The differential probability in the nuclear energy for the $2p\sigma_u$ channel is shown in fig. 4.6.
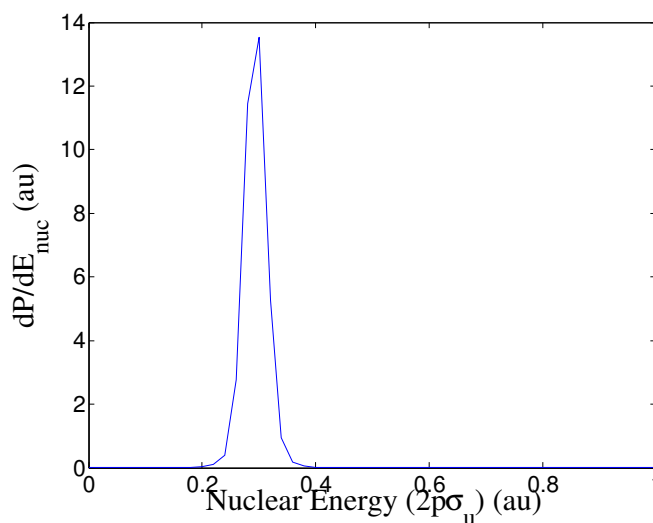
Figure 4.6: Differential probability on the nuclear energy for the $2p\sigma_u$ curve.
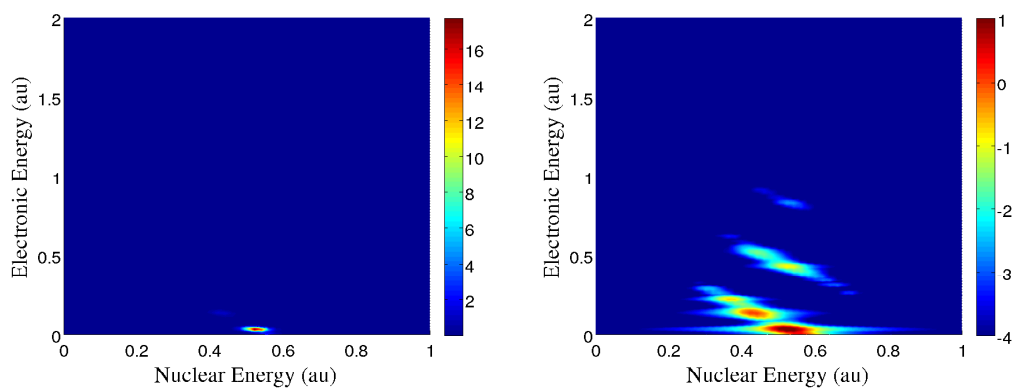
Figure 4.7: Same as in fig. 4.3 but for $\Omega = 0.398$ a.u..

There is a peak at 0.29 a.u. on the nuclear energy, which corresponds to being at $R = 2.0$ a.u. in the $2p\sigma_u$ curve. This confirms that we have a resonant transition between the $1s\sigma_g$ and $2p\sigma_u$ channel at the internuclear distance. The doubly differential probability is shown in fig. 4.7, again in linear and logarithmic scale.
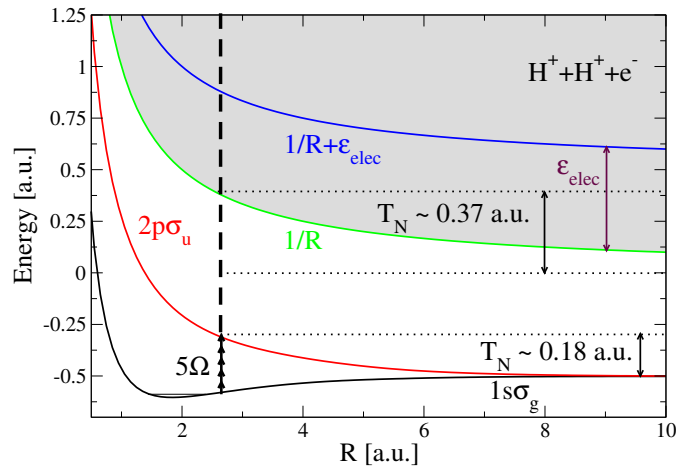
Figure 4.8: Same as fig. (4.2) for $\Omega = 0.0569\,a.u.$. The black arrows represent the absorption of five photons at $R = 2.65$ a.u.
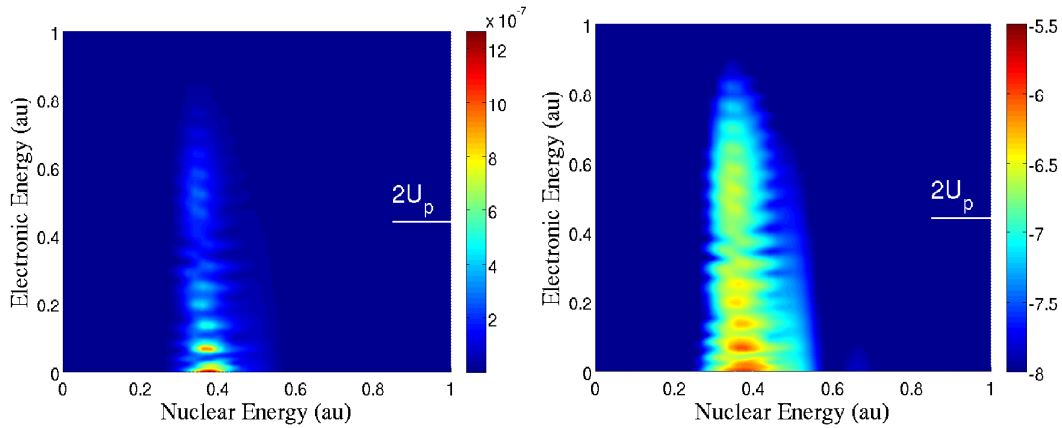
Figure 4.9: Same as in fig. 4.3 but for $\Omega = 0.0569$ a.u.

4.2.3 Infrared laser pulse

Finally, we show results for an IR pulse with $\Omega = 0.0569$ a.u., which corresponds to a 800 nm wavelength for the same pulse duration (16 fs) and intensity (10^{14} W/cm^2) as in the previous cases.. The doubly differential probability is shown in fig. 4.9.

In fig. 4.9, we observe several features: The first is that the most populated nuclear energies are no longer in the Franck-Condon region. This can be explained by the fact that at $R = 2.65$ a.u. we have a resonant transition to the $2p\sigma_u$, see fig. 4.8. Indeed, the nuclear differential probability at fig. 4.10, shows a peak at $E = 0.18$ a.u. that corresponds exactly to $R = 2.65$ a.u. in the $2p\sigma_u$ curve. The same internuclear position will lead to $E = 1/R = 0.37$ a.u. in the Coulomb explosion
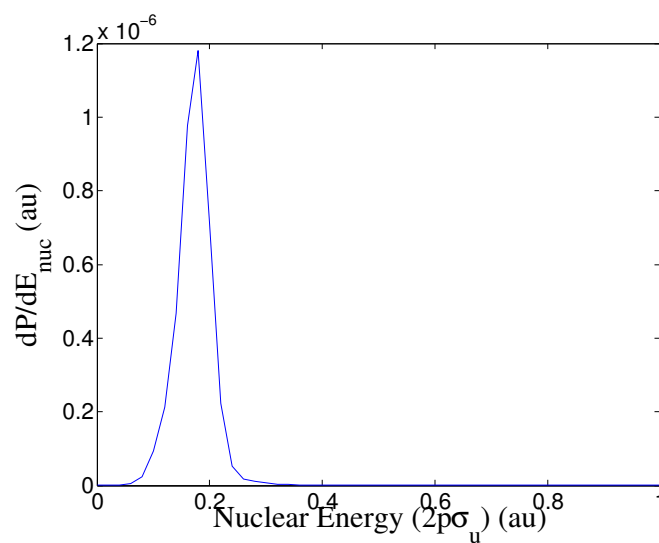
Figure 4.10: Differential probability on the nuclear energy for the $2p\sigma_u$ curve for $\Omega = 0.0569$ a.u.
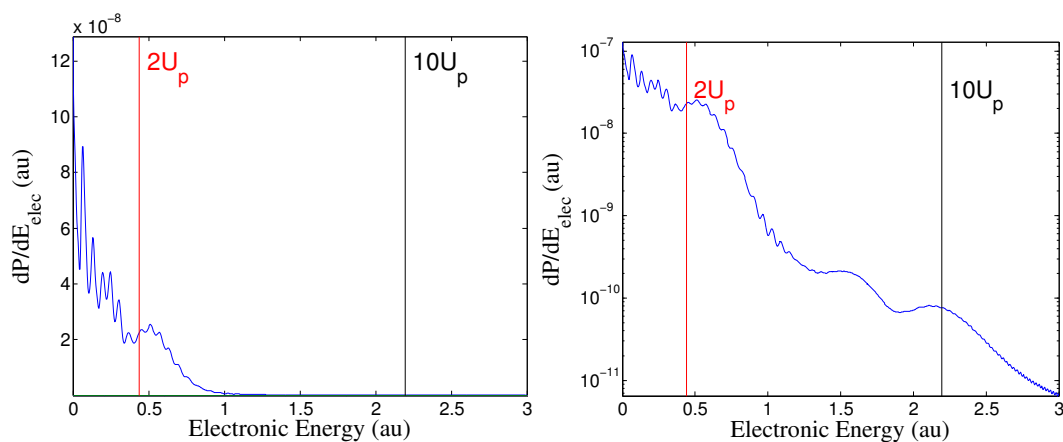
Figure 4.11: Photoelectron spectrum in linear scale (left) and in log scale (right) for $\Omega = 0.0569$ a.u.
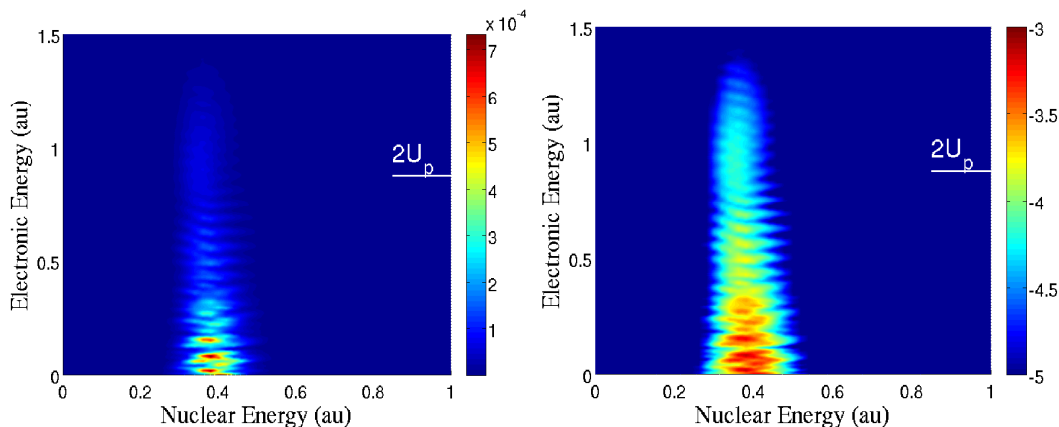
Figure 4.12: Same as in fig. 4.3 but for $\Omega = 0.0569$ a.u. photon, with peak intensity $I = 2 \times 10^{14}\,\mathrm{W/cm^2}$.
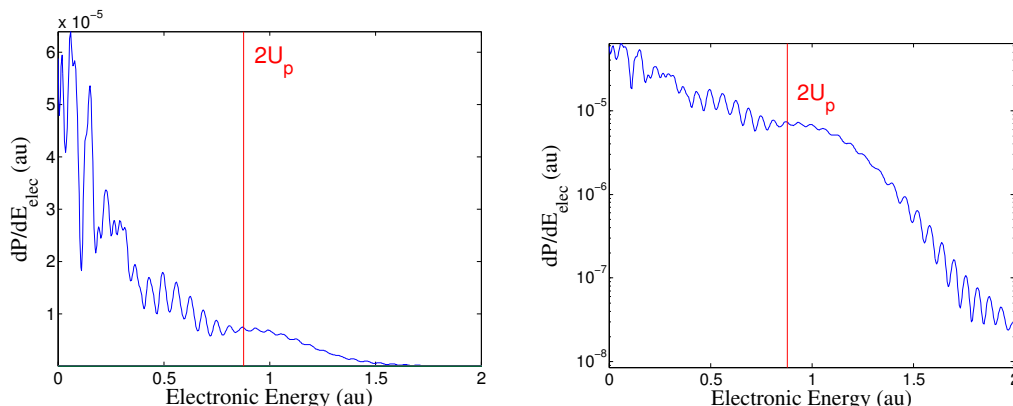
Figure 4.13: Photoelectron spectrum in linear scale (left) and in log scale (right) for $\Omega = 0.0569$ a.u. and with a peak intensity $I = 2 \times 10^{14}\,\mathrm{W/cm^2}$.

curve, that is the energy observed in the spectrum in fig. 4.9. The photoelectron spectrum can be obtained by integration in the nuclear energy of the 2D spectrum, and it is shown in fig. 4.11. This plot shows the typical structure observed for the ATI peaks in atoms [11]. Two plateaus are observed around $2U_p$ and $10U_p$, plus a third "shoulder" in between them.

A striking feature is that until $2U_p$, the lines in the 2D spectrum are horizontal. They start to become tilted with slope -1 for electron energies higher than $2U_p$. In general, we expect that the energy conservation lines have slope -1. To be sure that there a regime transition around $2U_p$, we have performed a calculation where we double the intensity and we keep the same photon energy. These results are shown in figs. 4.12 and 4.13.

The values of $2U_p$ and $10U_p$ have a physical meaning in ATI spectra. Until $2U_p$, the photoelectron spectrum is dominated by direct electrons [41], electrons that after ionization do not recollide

with the nuclei. Between $2U_p$ and $10U_p$ the photoelectron spectrum is dominated by the rescattered electrons, which are electrons that after entering in the continuum, are driven back to the nuclei and rescattered by it. In this picture, electrons are born in the continuum by tunnel ionization and with zero velocity. Direct electrons emitted from two different equilibrium distances will gain the same kinetic energy, since it does not depend on the nuclear distance. This will appear in the contour plot as horizontal lines, as we obtain in both calculations. For rescattered electrons, energy must be conserved after the collision of the electron with the nuclei so the fringes must lie on energy conservation lines with slope -1, thus the tilted lines for $E_e > 2U_p$.

Chapter 5

Autoionization in the H_2 molecule

"It is often stated that of all the theories proposed in this century, the silliest is quantum theory. In fact, some say that the only thing that quantum theory has going for it is that it is unquestionably correct."

Michio Kaku

5.1 Theory

In this Chapter, we study H_2 autoionization by means of a close-coupling method. Such method has already been extensively detailed in the literature [13–20]. We will present results for H_2 photoionization with an APT-pump-IR-probe scheme. We will focus on the autoionization dynamics of the molecule.

5.1.1 Time-dependent Schrödinger equation

We will treat the electric field as a classical field, in the so-called semi-classical approximation, and the electrons and nuclei with non-relativistic quantum mechanics. We will also neglect mass polarization terms in the molecular Hamiltonian. Based on these approximations we have that the TDSE reads (in atomic units)

$$\left[\hat{H}_0\left(\boldsymbol{r}, R\right) + \hat{V}\left(t\right) - i\frac{\partial}{\partial t} \right] \Phi\left(\boldsymbol{r}, R, t\right) = 0 \tag{5.1.1}$$

where $\boldsymbol{r}$ stands for the electronic coordinates ($\boldsymbol{r}_1$ and $\boldsymbol{r}_2$) and R for the internuclear distance. $\hat{H}_0$ is the molecular Hamiltonian for molecular hydrogen. The interaction term is written on the dipole approximation and in this calculations we will use the velocity gauge. Thus

$$\hat{V}\left(t\right) = \left(\hat{\vec{p}}_1 + \hat{\vec{p}}_2\right) \cdot \vec{A}\left(t\right) \tag{5.1.2}$$

where $\hat{\vec{p}}_i$ is the canonical momentum of electron i and $\vec{A}\left(t\right)$ is the vector potential. The electric field is $\vec{E}\left(t\right) = -\partial_t \vec{A}\left(t\right)$. We will solve the TDSE with a spectral method in which we expand our time-dependent wavefunction in a basis of molecular eigenstates. This is quite convenient for the extraction of observables, since the coefficients of the wavefunction have a direct physical meaning.

5.1.2 Molecular Bound Eigenstates

We will work under the Born-Oppenheimer (BO) approximation. Under this approximation we assume that a BO eigenstate is a real eigenstate of the Molecular Hamiltonian. The Molecular Hamiltonian is

$$\hat{H}_0 = -\frac{\nabla_R^2}{2\mu} + \hat{H}_{el}, \tag{5.1.3}$$

$$\hat{H}_{el} = -\frac{\nabla_{\boldsymbol{r}_1}^2}{2} - \frac{\nabla_{\boldsymbol{r}_2}^2}{2} + \hat{V}_{ee} + \hat{V}_{NN} + \hat{V}_{eN}, \tag{5.1.4}$$

where μ is the reduced mass of the two protons, $\hat{V}_{ee}$ is the Coulomb interaction term between the electrons, $\hat{V}_{eN}$ is the Coulomb interaction term between the electrons and nuclei and $\hat{V}_{NN}$ is the Coulomb interaction term between the nuclei. The electronic wavefunction obeys the following equation

$$\left[\hat{H}_{el} - E_i^{el}\left(R\right)\right] \Psi_i\left(\boldsymbol{r}_1, \boldsymbol{r}_2; R\right) = 0. \tag{5.1.5}$$

where $E_i^{el}\left(R\right)$ is the ith electronic curve.

We can expand a molecular eigenstate as a sum of electronic wavefunctions in which the coefficients depend on R:

$$\Phi\left(\boldsymbol{r}_1, \boldsymbol{r}_2, R\right) = \sum_i \chi_i\left(R\right) \Psi_i\left(\boldsymbol{r}_1, \boldsymbol{r}_2; R\right), \tag{5.1.6}$$

where

$$\hat{H}_0 \Phi \left(\boldsymbol{r}_1, \boldsymbol{r}_2, R \right) = E \Phi \left(\boldsymbol{r}_1, \boldsymbol{r}_2, R \right). \tag{5.1.7}$$

Replacing (5.1.6) into equation (5.1.7) and projecting into an electronic wavefunction $\Psi_j \left(\boldsymbol{r}_1, \boldsymbol{r}_2; R \right)$ we obtain

$$\left[-\frac{\nabla_R^2}{2\mu} + E_j^{el} \left(R \right) - E \right] \chi_j \left(R \right) = \frac{1}{2\mu} \sum_{i \neq j} O_{ji} \chi_i \left(R \right) \tag{5.1.8}$$

where

$$O_{ji} = 2a_{ji} \cdot \nabla_R + \nabla_R \cdot a_{ji} - b_{ji}, \tag{5.1.9}$$

$$a_{ji} = \int \Psi_j \left(\boldsymbol{r}_1, \boldsymbol{r}_2; R \right) \nabla_R \Psi_i \left(\boldsymbol{r}_1, \boldsymbol{r}_2; R \right) d\boldsymbol{r}_1 d\boldsymbol{r}_2, \tag{5.1.10}$$

$$b_{ji} = \int \left(\nabla_R \Psi_j \left(\boldsymbol{r}_1, \boldsymbol{r}_2; R \right) \right) \cdot \left(\nabla_R \Psi_i \left(\boldsymbol{r}_1, \boldsymbol{r}_2; R \right) \right) d\boldsymbol{r}_1 d\boldsymbol{r}_2. \tag{5.1.11}$$

where O_{ji} is the non-adiabatic operator that couples distinct electronic states [42].

Note that equation (5.1.8) is fully equivalent to the full time-independent Schrödinger equation. The Born-Oppenheimer approximation states that the non-adiabatic operator O_{ji} is zero, which implies that the gradient over the nuclear coordinates of an electronic function is zero. Then, the nuclear Schrödinger equation for the a diatomic molecule is:

$$\left[-\frac{1}{2\mu} \frac{d^2}{dR^2} + \frac{J \left(J + 1 \right)}{2\mu R^2} + E_j^{el} \left(R \right) - E \right] \chi_j \left(R \right) = 0 \tag{5.1.12}$$

where J is the rotational quantum number. We have assumed here that the nuclear wavefunction is the product of a radial wavefunction, $\chi_j \left(R \right)$, and a spherical harmonic, since the potential is central. We will neglect rotational effects and take $J = 0$. For each electronic curve we will obtain a set of vibrational states, ν_j. The vibronic wavefunctions are the molecular eigenstates in the Born-Oppenheimer approximation, and form a complete basis set $\{ \Psi_i \left(\boldsymbol{r}_1, \boldsymbol{r}_2; R \right) \chi_{\nu_i} \left(R \right) \}$ with a vibronic energy $E = W_{\nu_i}$.

5.1.3 Resonant states

It was back on 1961 when Ugo Fano published a fundamental paper for Atomic and Molecular Physics [43]. In this paper, Fano explained the autoionization of the He atom in terms of a doubly

excited state immersed in a continuum. This phenomenon, autoionization, can only be explained if we take into account correlation effects in the electronic structure. An additional complication is found in molecules, such as H_2, since the lifetime of each resonant state depends on the nuclear configuration.

We will treat autoionization within the Feshbach theory [44]. We start by defining the P subspace, which contains the non-resonant states. Thus, $1 - P = Q$ is a complementary subspace which contains the resonant states. Since we are working in the Born-Oppenheimer approximation, we will have a basis of molecular eigenstates in each subspace. These states will not be true eigenfunctions of the electronic and nuclear Hamiltonian. In this way, these states will be coupled during the time evolution, even when the interaction term with the electromagnetic field is zero. The projection operators on these subspaces satisfy the relations:

$$\hat{P} + \hat{Q} = 1 \tag{5.1.13}$$

$$\hat{P}\hat{Q} = 0 \tag{5.1.14}$$

$$\hat{P}^2 = \hat{P} \tag{5.1.15}$$

$$\hat{Q}^2 = \hat{Q}. \tag{5.1.16}$$

The unperturbed Hamiltonian can be written as

$$\hat{H}_0 = \hat{Q}\hat{H}_0\hat{P} + \hat{P}\hat{H}_0\hat{Q} + \hat{P}\hat{H}_0\hat{P} + \hat{Q}\hat{H}_0\hat{Q} \tag{5.1.17}$$

The non-resonant states, $\left\{ \Psi_\alpha^{\varepsilon,l} \left(\boldsymbol{r}; R \right) \chi_{\nu_\alpha} \left(R \right) \right\}$, where ε stands for the electron energy in the continuum and l stands for the angular momentum, will obey the projected electronic equation

$$\left[\hat{P}\hat{H}_{el}\hat{P} - \mathcal{E} \left(R \right) \right] \Psi_\alpha^{\varepsilon,l} \left(\boldsymbol{r}; R \right) = 0, \quad \mathcal{E} \left(R \right) = E_\alpha \left(R \right) + \varepsilon \tag{5.1.18}$$

where α stands for the electronic curve of the ion of H_2^+. Notice that this idea is equivalent to making copies of the electronic curve by summing the energy of the electron in the continuum. It will also appear in the Resolvent Technique, Chapter 4. The nuclear wavefunction, $\chi_{\nu_\alpha} \left(R \right)$, satisfies

$$\left[-\frac{1}{2\mu} \frac{d^2}{dR^2} + \mathcal{E} \left(R \right) - W_{\nu_\alpha} \right] \chi_{\nu_\alpha} \left(R \right) = 0, \tag{5.1.19}$$

where W_{ν_α} is the vibronic energy. In a similar way, the resonant states will satisfy a projected electronic equation

$$\left[\hat{Q} \hat{H}_{el} \hat{Q} - \mathcal{E}_r (R) \right] \phi_r (\mathbf{r}; R) \;=\; 0 \tag{5.1.20}$$

and the corresponding nuclear equation

$$\left[-\frac{1}{2\mu} \frac{d^2}{dR^2} + \mathcal{E}_r (R) - W_{k_r} \right] \chi_{k_r} (R) = 0 \tag{5.1.21}$$

where r stands for the resonant electronic state, and $\mathcal{E}_r (R)$ is the corresponding electronic curve.

5.1.4   Propagation

Once the molecular basis set has been obtained, we can insert it in the TDSE and propagate it in time. The molecular wavefunction can be expanded as a sum over molecular bound states, resonant states and continuum electronic states:

$$\Phi (\mathbf{r}, R, t) \;=\; \sum_n \sum_{\nu_n}\!\!\!\!\!\!\int C_{n\nu_n} (t) \, \Psi_{n\nu_n} (\mathbf{r}, R) \, e^{-iW_{n\nu_n} t} \tag{5.1.22}$$

$$+ \sum_r \sum_{\nu_r}\!\!\!\!\!\!\int C_{r\nu_r} (t) \, \Psi_{r\nu_r} (\mathbf{r}, R) \, e^{-iW_{r\nu_r} t} \tag{5.1.23}$$

$$+ \sum_{\alpha, l_\alpha} \int d\varepsilon_\alpha \sum_{\nu_\alpha}\!\!\!\!\!\!\int C_{\alpha\varepsilon_\alpha\nu_\alpha}^{l_\alpha} (t) \, \Psi_{\alpha\varepsilon_\alpha\nu_\alpha}^{l_\alpha} (\mathbf{r}, R) \, e^{-iW_{\alpha\varepsilon_\alpha} t}. \tag{5.1.24}$$

Inserting this ansatz in the TDSE we obtain a set of coupled first order differential equations. The system can be written as

$$i \begin{pmatrix} \dot{C}_{n\nu_n} \\ \dot{C}_{r\nu_r} \\ \dot{C}_{\alpha\varepsilon_\alpha\nu_\alpha}^{l_\alpha} \end{pmatrix} = \begin{pmatrix} \vec{A}(t) \, p_{n'\nu_n',n\nu_n} & \vec{A}(t) \, p_{n\nu_n,r\nu_r} & \vec{A}(t) \, p_{n\nu_n,\,\alpha\varepsilon_\alpha\nu_\alpha}^{l_\alpha} \\ \vec{A}(t) \, p_{r\nu_r,n\nu_n} & \vec{A}(t) \, p_{r'\nu_r',r\nu_r} & \left(\hat{Q}\hat{H}_0\hat{P} + \vec{A}(t) \, p \right)_{r\nu_r,\,\alpha\varepsilon_\alpha\nu_\alpha}^{l_\alpha} \\ \vec{A}(t) \, p_{\alpha\varepsilon_\alpha\nu_\alpha,n\nu_n}^{l_\alpha} & \left(\hat{P}\hat{H}_0\hat{Q} + \vec{A}(t) \, p \right)_{\alpha\varepsilon_\alpha\nu_\alpha,r\nu_r}^{l_\alpha} & \vec{A}(t) \, p_{\alpha'\varepsilon_{\alpha'}\nu_{\alpha'},\,\alpha\varepsilon_\alpha\nu_\alpha}^{l_{\alpha'},\,l_\alpha} \end{pmatrix}$$

$$\times \begin{pmatrix} C_{n\nu_n} \\ C_{r\nu_r} \\ C_{\alpha\varepsilon_\alpha\nu_\alpha}^{l_\alpha} \end{pmatrix} \tag{5.1.25}$$

where $p_{\alpha,\beta}$ is the matrix element $\langle \alpha | \hat{p} | \beta \rangle$. This system of differential equations is solved by imposing an initial condition that is the initial state of the system, a bound state of the molecular hydrogen or a linear combination of them.

The advantage of this method is that we can turn off some couplings and in this way evaluate the influence of that states comparing with a full calculation.

Our molecular eigenstates are not really eigenstates of the Hamiltonian, so we must be careful. Since the couplings $\hat{P}\hat{H}_0\hat{Q}$ and $\hat{Q}\hat{H}_0\hat{P}$ will couple different states even after the end of the pulse, we must perform the propagation until $t_{prop} > t_{pulse} + T_{AI}$, where t_{pulse} is the duration of the pulse and T_{AI} the largest autoionization time of the resonances involved in the calculation, to ensure that all the doubly excited states have had time to decay at the end of the propagation.

5.1.5 Extraction of observables

As stated before, working on a spectral method has the great advantage that at the end of the propagation, we can easily extract the physical observables, since each coefficient is the probability amplitude of a well defined state. The transition probability to each state can be evaluated at t_{prop} as the modulus square of the corresponding coefficient.

We are now ready to write the physical observables that we will use in the following analysis. The probability density of finding an electron in the electronic channel α, with energy ε_α and with a vibrational energy ν_α is given by

$$\frac{d^2 P_{\alpha,\nu_\alpha,\varepsilon_\alpha}(t)}{d\varepsilon_\alpha d\nu_\alpha} = \sum_{l_\alpha} \left| C^{l_\alpha}_{\alpha\varepsilon_\alpha\nu_\alpha}(t) \right|^2. \tag{5.1.26}$$

If we want the quantity measured in an experiment, the doubly differential probability as a function of the photoelectron energy and the proton kinetic energy, we must perform a sum over all the α channels

$$\frac{d^2 P_{E_{H+},\varepsilon}(t)}{d\varepsilon dE_{H+}} = \sum_{\alpha} \sum_{l_\alpha} \left| C^{l_\alpha}_{\alpha\varepsilon_\alpha\nu_\alpha}(t) \right|^2. \tag{5.1.27}$$

To obtain the photoelectron spectra we must perform an integration over the vibrational levels ν_α. The electron kinetic energy spectrum (EKE) can be calculated as

$$\frac{dP_{\varepsilon_\alpha}(t)}{d\varepsilon} = \sum_{\alpha} \oint_{\nu_\alpha} \sum_{l_\alpha} \left| C^{l_\alpha}_{\alpha\varepsilon_\alpha\nu_\alpha}(t) \right|^2. \tag{5.1.28}$$

We will also calculate the proton kinetic energy spectrum (PKE), that can be obtained with

$$\frac{dP_{E_{H+}}(t)}{dE_{H+}} = \sum_{\alpha} \sum_{\varepsilon_\alpha} \sum_{l_\alpha} \left| C^{l_\alpha}_{\alpha\varepsilon_\alpha\nu_\alpha}(t) \right|^2. \tag{5.1.29}$$

5.2 Results

In this work we use a pump-probe scheme to study the dynamics of the Q_1 doubly excited states of the H_2 molecule with $^1\Sigma_u^+$ symmetry. We use an APT field as pump, with an intense harmonic reaching the first Q_1 $^1\Sigma_u^+$ resonance in a vertical transition from the molecular groundstate. The probe is a near-IR pulse used to track the autoionization dynamics. Since we are working on a spectral method, we can perform calculations including the Q_1 $^1\Sigma_u^+$ states and another in which these states are removed from the calculation. We will compare both calculations to evaluate the influence of the Q_1 $^1\Sigma_u^+$ resonances. This work has lead to publication [21].

5.2.1 Born-Oppenheimer curves of H_2 molecule

The Born-Oppenheimer curves for the H_2 molecule are shown in fig. 5.1. The figure shows the H_2 molecular groundstate and the two first electronic curves for the $H_2{}^+$ molecule, $1s\sigma_g$ and $2p\sigma_u$. The first series of doubly excited states, Q_1 is shown in red (Σ_g^+ symmetry) and in blue (Σ_u^+ symmetry). All the potential curves of the Q_1 series lead to a dissociative path, since they are repulsive. These resonant states will lead to dissociation into two neutral atoms ($H_2^{**} \to H + H$) or ions ($H_2^{**} \to H + H$) or decay to the non-dissociative ($H_2^{**} \to H_2{}^+ + e^-$) or dissociative ($H_2^{**} \to H^+ + H + e^-$) continuum.

We are working under the dipole approximation and with linearly polarized light along the internuclear axis. If our initial symmetry is the symmetry of the H_2 groundstate, $^1\Sigma_g^+$, we can only populate states with symmetry $^1\Sigma_g^+$ (by absorption of an even number of photons) or $^1\Sigma_u^+$ (by absorption of an odd number of photons).

We must emphasize the fact that this set-up can excite our molecule in a vertical transition to the first Q_1 $^1\Sigma_u^+$ resonance via one-photon absorption (with harmonic H19). On the other hand, the Q_1 $^1\Sigma_g^+$ resonance can only be populated by a two-photon absorption, since the molecule must absorb an even number of photons.

We will focus our attention in the dissociative ionizing channel of the Q_1 $^1\Sigma_u^+$. This process, $H_2^{**} \to H + H^+ + e^-$, can be monitored by two observables, the photoelectron energy spectrum (EKE) and the proton kinetic energy spectrum (PKE).

We have performed three types of calculations: one where all states included, one where we remove the Q_1 $^1\Sigma_u^+$ resonances, and another one where we remove the Q_1 $^1\Sigma_g^+$ resonances. We have concluded that the influence of the Q_1 $^1\Sigma_g^+$ resonances is negligible, so we will focus our attention
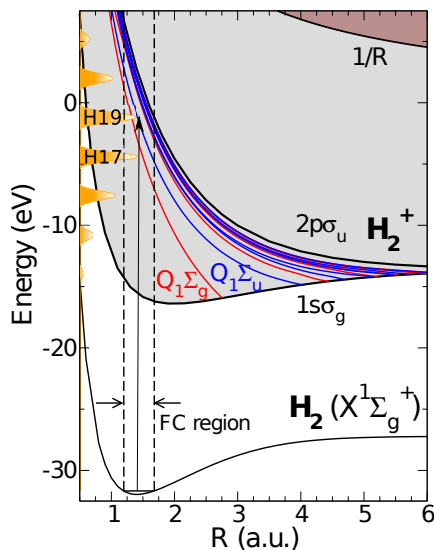
Figure 5.1: Born-Oppenheimer potential energy curves for the H_2 molecule. The spectrum of the APT pulse is shown in orange and it has his origin at the groundstate of the H_2 molecule. The grey zone corresponds to ionization. The Franck-Condon region is also showed. The black vertical arrow corresponds to a vertical transition between the groundstate of the H_2 and the first $Q_1 \, {}^1\Sigma_u^+$ resonance at the equilibrium internuclear distance ($R = 1.4$ a.u.).

on the former two cases.

The dominant process will be the single ionization of the H_2 molecule. This process leads mainly to the $1s\sigma_g$ electronic state, since only the harmonic H23 has sufficient energy to reach the $2p\sigma_u$ curve. Besides, the dominant process is the non-dissociative ionization to the $1s\sigma_g$ electronic state ($H_2 \rightarrow H_2^+ \, (1s\sigma_g) + e^-$), so the EKE will be dominated by electrons coming from this channel and the influence of the resonances will be much clearer in the PKE.

5.2.2 Laser pulse

To study the $Q_1 \, {}^1\Sigma_u^+$ resonances, we use an APT-pump-IR-probe set-up. The APT is formed by a train of four XUV pulses with FWHM = 200 as and frequency 17ω, where $\omega = 1.605$ eV is the frequency of the generating IR field. The delay between the pulses in the train is $\delta t = T/2$, where T is the IR period, which origins an energy spectrum with two principal harmonics at frequencies 17ω and 19ω that can be observed at fig. 5.1. We will denote these two harmonics by H17 and H19, respectively. The less intense harmonics will be denoted by H13, H15, H21 and H23. The parameters of the APT pulse are choosen such that the $Q_1 \, {}^1\Sigma_u^+$ series is significantly populated. The intensity of the two central pulses is 10^9 W/cm² and 0.35×10^9 W/cm² for the external pulses,
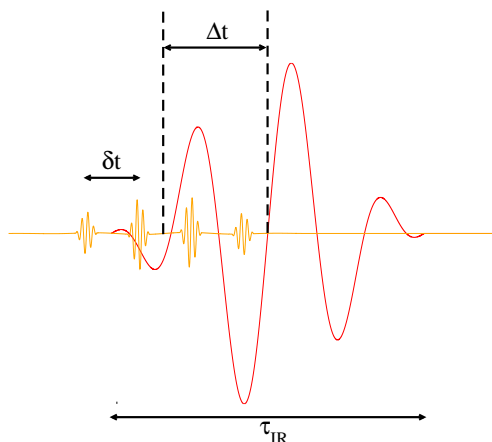
Figure 5.2: Schematic picture of the pump-probe scheme used. The red line represents the IR electric field and the orange one the APT field. Both are represented in an arbitrary scale, and the APT is scaled to become visible.

which corresponds to an APT envelope with FWHM = 3 fs and $I = 1.14 \times 10^9$ W/cm². The IR probe ($\omega = 1.605$ eV), which can also be used to generate the above APT, has a duration of three optical cycles, a sin-square envelope and a peak intensity of 10^{12} W/cm². To probe the dynamics of autoionization we will perform a scan in delays between the pump and probe pulses. The delay Δt is defined with respect to the center of their corresponding envelopes, and $\Delta t > 0$ means that the APT comes before the IR pulse, see fig. 5.2. For $\Delta t = 0$, the XUV pulses are located at maxima and minima of the IR field.

5.2.3   Doubly differential photoelectron-proton kinetic energy spectra

The calculated doubly differential photoelectron proton kinetic energy spectra obtained by using the APT-pump-IR-probe scheme described in the previous section are shown in fig. 5.3. For comparison, the figure also shows the results obtained with a Single Attosecond Pulse (SAP) and no IR pulse. This kind of representation, although difficult to achieve experimentally, contains very rich information on the photoionization dynamics, since it describes how energy is shared between electrons and nuclei. The dashed lines in the figure represent energy conservation for different harmonic frequencies: for a given XUV photon energy $\hbar\omega$, where ω is the XUV photon frequency, the excess energy E_ω can be written as $E_\omega = \hbar\omega - (E_\infty - E_{\nu_0}) = \hbar\omega - 18.1$ eV, where E_{ν_0} is the energy of the groundstate of H_2 molecule ($E_{\nu_0} = -31.7$ eV) and E_∞ is the energy needed to reach the ionization threshold which is the groundstate energy for the hydrogen atom ($E_\infty = -13.6$ eV). The lines go from EKE=E_ω and zero PKE to zero EKE and PKE=$E_\omega/2$.
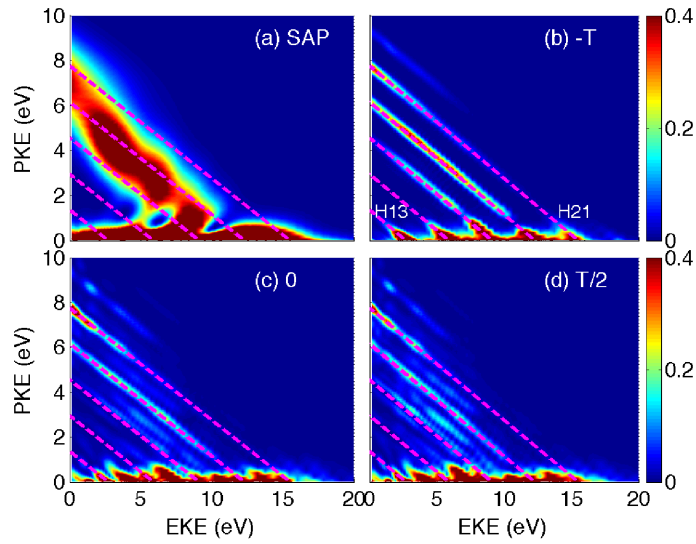
Figure 5.3: Doubly differential photoelectron-proton kinetic energy spectrum for a SAP (a) and for an APT+IR with three different time delays: $\Delta t = -T$ (b), $\Delta t = 0$ and $\Delta t = T/2$ (d), where T is the period of the IR field. The magenta dashed lines represents the lines of energy conservation for the different harmonics. The uppermost line corresponds to the H21 and the bottom one to the H13.

In the result shown in 5.3(a) for a single attosecond pulse (SAP), one can distinguish two well defined regions: the first one, in which probabilities are largest, corresponds to very slow protons (direct ionization from $1s\sigma_g$), and the second one around the energy conservation lines for intermediate proton energies (autoionization from the DESs). When the IR pulse comes before the APT, (5.3(b), delay $\Delta t = -T$), the 2D spectrum exclusively reflects the effect of the APT. This is because the IR pulse is not intense enough to induce ionization or electronic excitation in H_2 through multiphoton absorption. Thus, for all practical purposes, when the XUV APT arrives, the H_2 molecule is still in its ground state. After absorption of the XUV photons, a substantial part of the excess energy goes again to the electrons and leads to the pronounced signal at low proton energies. Nevertheless, this signal exhibits clear structures that follow the energy conservation lines that represent the expected final energies upon ionization by the harmonics from E_{21} (uppermost line) down to E_{13}. Along these energy conservation lines and for intermediate proton energies, the ionization probability is also high, which is entirely due to autoionization of the DESs that have been populated by the XUV photon. Besides, at the highest proton energies and very small EKE, there is a signature of direct photoionization into the $2p\sigma_u$ continuum. Therefore, the 2D spectrum of 5.3(b) reflects exactly the same features as those of 5.3(a) for the SAP, but only along the energy conservation lines that correspond to the different harmonic energies.
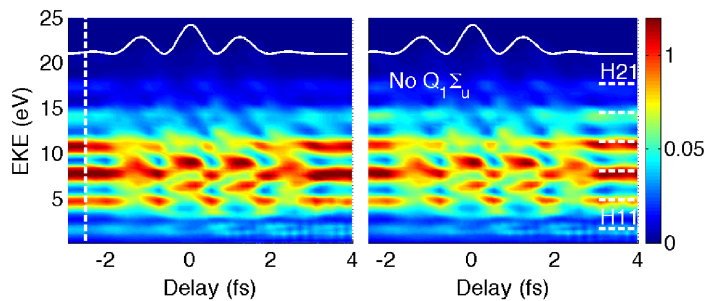
Figure 5.4: Photoelectron spectrum for the full calculation (left) and the calculation without the $Q_1\,{}^1\Sigma_u^+$(right). The result without the IR field (only the APT field) is shown on the left of the vertical dashed line, only for the full calculation. The expected final energy after absorbing an odd harmonic is showed at left. The square of the vector potential of the IR field is shown in the upper part of both plots. All probabilities are multiplied by 10^6.

When the APT and IR fields overlap, the APT drives first the system into the continuum whence absorption or emission of few IR photons is now possible. The latter processes lead to final energies right in the middle between the harmonic bands. The resulting sidebands are clearly visible for Δt=0 (c), and $T/2$ (d). Indeed, as mentioned above, DESs have repulsive energy curves (see 5.1). Therefore, when one of these states is populated by an XUV photon, the molecule starts to increase its internuclear distance, and it can either lead to dissociation into two neutral atoms or decay into the ionization continuum. The longer the molecule has evolved in the dissociating curve, the higher will be the kinetic energy gained by the nuclei. Consequently, the higher the proton energy in a given energy-conservation line, the larger the autoionization lifetime of the DES.

Although these 2D PKE-EKE spectra are very useful to understand the photoionization process, it is much more feasible experimentally to obtain integrated photoelectron and proton kinetic energy spectra. We show results for both in the next two subsections.

5.2.4   Photoelectron spectrum (EKE)

We will show the EKE spectrum in a 2D plot in fig. 5.4, for a scan in time delays.

The vertical lines for the harmonics are calculated by taking the difference between the ground-state energy of the H_2 molecule and the energy of the $\nu = 2$ vibrational state of the $1s\sigma_g$ curve which is, together with $\nu = 3$, the most populated. Since we can end up in higher vibrational states, this energy will be only an upper bound to the energy of the electron after the absorption of an XUV photon.
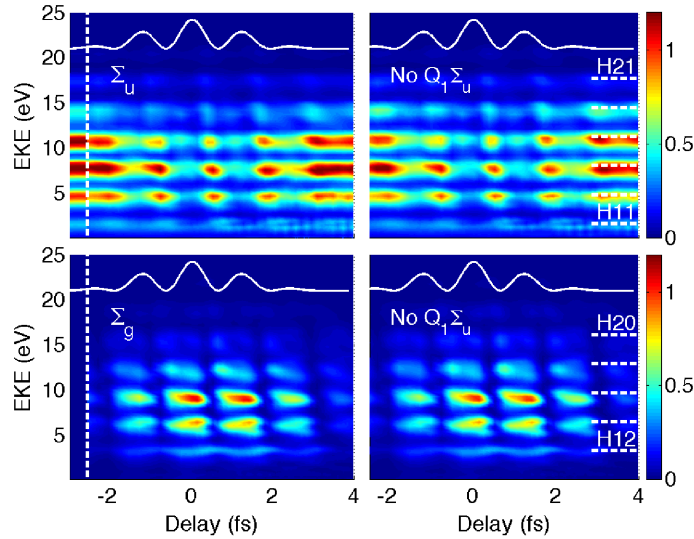
Figure 5.5: Same as in fig. 5.4, but split into total symmetry Σ_u (top figures) and Σ_g (bottom figures).

The first thing that we can immediately observe is that there is no significant difference between the two calculations. This was expected, since the dominant contribution to the EKE is coming from non-dissociative ionization.

We will first analyse the two limit cases: when $\Delta t \ll$ FWHM, we expect that the IR field, since it is coming first, will not induce any photoionization. This case can be reduced to the case where there is only an APT. The other limit case is when $\Delta t \gg$ FWHM, where there is no overlap between the APT pulse and the IR field. The ejected electron is not affected by the IR field and in this way we will obtain the same result that when $\Delta t \ll$ FWHM . Since when the IR field arrives the electron is already at a significant distance from the nuclei, the IR field can not induce photon absorption or emission. When both pulses overlap, $(\Delta t \sim 0)$, the molecule is first ionized by an XUV photon and after that it can emit or absorb IR photons, resulting in the appearance of sidebands located at even harmonics of the generating frequency. A periodicity of $T/2$ is observed for the resulting bands and sidebands being in opposition of phase. This has already been observed for atoms [45] and also theoretical explained [46, 47].

In order to understand the dynamics of this process we can split the EKE spectra into contributions from different symmetries: Σ_u and Σ_g. This is shown in fig. 5.5: the top two figures show the ionization probabilities for the Σ_u symmetry, and the bottom figures show the Σ_g symmetry. Note the periodicity in both cases is $T/2$. When the transition probability to the sidebands is maximized, there is a depletion in the odd harmonic bands. The combination of these two clear patterns (Σ_g and Σ_u) produces the complicated pattern observed in the total photoelectron
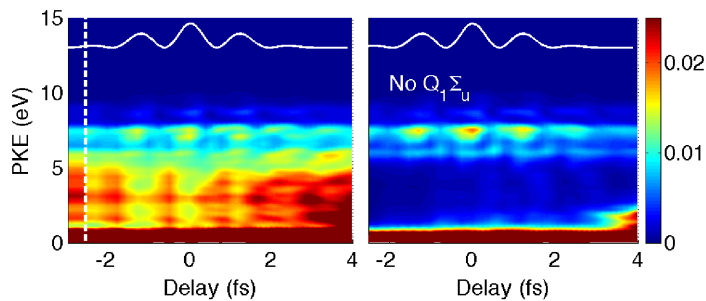
Figure 5.6: Proton kinetic energy spectrum for the full calculation (left) and the calculation without the Q_1 $^1\Sigma_u^+$(right). The result without the IR field (only the APT field) is shown on the left of the vertical dashed line, only for the full calculation. The expected final energy after absorbing an odd harmonic is showed at left. The square of the vector potential of the IR field is shown in the upper part of both plots. All probabilities are multiplied by 10^6.

spectra.

As expected, the photoelectron spectrum do not provides any information about the autoionization process. This is due to the fact that the dominant part in the EKE is non-dissociative ionization.

5.2.5 Proton kinetic energy spectrum (PKE)

Since the EKE spectrum does not reveal any signature of the DES, we will analyse the PKE spectrum. Results are shown in the fig. 5.6 for the full calculation (left) and without the Q_1 $^1\Sigma_u^+$ resonances (right). We can see in both figures that at low proton energies ($< 1\,\text{eV}$) there is a very intense probability. This corresponds to the direct ionization to the $1s\sigma_g$ channel. Also for both calculations, we can see a contribution at proton energies around $\sim 7.75\,\text{eV}$. This is due to the direct ionization to the $2p\sigma_u$ channel. We have already argued that to reach this channel in the Franck-Condon region we must go to energies higher than H21. For delays where $\Delta t > 3.5\,\text{fs}$, there is a enhancement of the probability for slow protons. This is due to bond softening: at these time delays, the nuclear wavepacket on the $1s\sigma_g$ channel evolves to higher internuclear distances (note that the equilibrium internuclear distance is larger for H_2^+ (2 a.u.) than for H_2 (1.4 a.u.)), so it can reach an internuclear distance where the transition between the $1s\sigma_g$ and the $2p\sigma_u$ curve is accessible upon absorption of a few IR photons. This was already observed in H_2 [48].

There is a clear difference between both calculations that can be related to the signature of the Q_1 $^1\Sigma_u^+$ resonances. It appears clearly at energies between $1 - 6\,\text{eV}$ with the same periodicity observed for the photoelectron spectrum. This signature disappears when the Q_1 $^1\Sigma_u^+$ are not
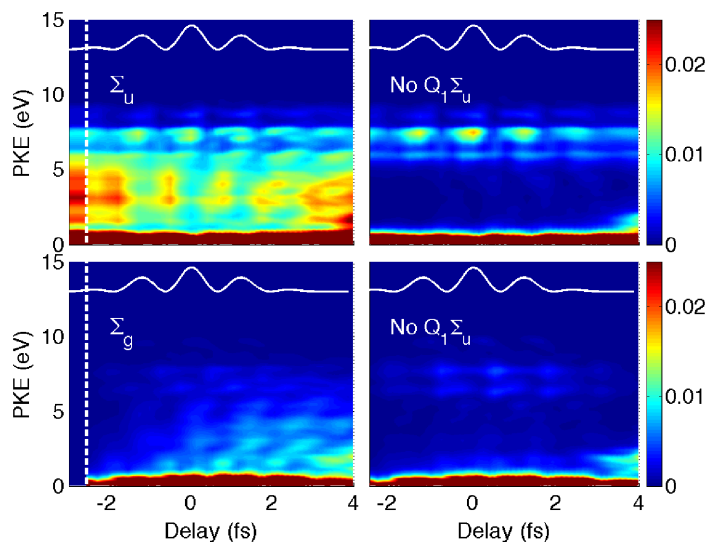
Figure 5.7: Proton kinetic energy spectrum for different final symmetries. The top figures are the Σ_u symmetry and the bottom figures the Σ_g symmetry. The figures have the same scheme as in fig. 5.6.

included in the calculation.

To understand better these results we split them again into final different symmetries, see fig. 5.7. In these spectra, we can observe that the major contribution to the signature of the autoionization decay from the $Q_1\,^1\Sigma_u^+$ is appearing in the Σ_u symmetry. For non-radiative decay, which is dominant, the $Q_1\,^1\Sigma_u^+$ resonances can only decay on the $1s\sigma_g$ channel with the same symmetry (Σ_u). If the decay is radiative, after absorption or emission of an IR photon, the symmetry changes and the final symmetry will be Σ_g.

The PKE spectrum for the $1s\sigma_g$ channel is plotted in fig. 5.8. Including only this channel eliminates the contributions of bond softening and the direct ionization to the $2p\sigma_u$ channel. Here we can see even more clearly the signature of the $Q_1\,^1\Sigma_u^+$ resonances.
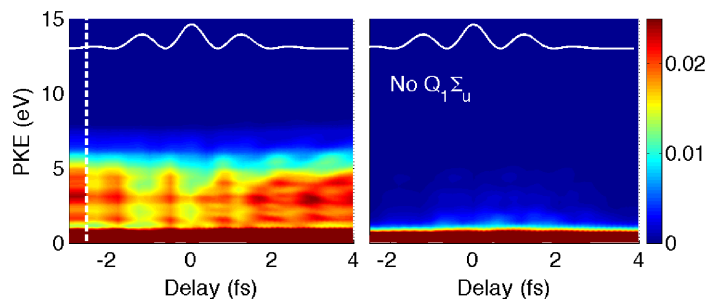
Figure 5.8: Same as in fig. 5.6, but including only the $1s\sigma_g$ channel.

Chapter 6

Conclusions

In this master thesis, we have used two main approaches to solve the TDSE for molecules interacting with ultrashort laser fields: a spectral method and a grid method. The spectral method was used to study the autoionization dynamics in the H_2 molecule and the grid method to study photoionization in the H_2^+ molecule. This distinction was made since grid methods, at present, are unfeasible for very high dimensional systems. On the other hand spectral methods are not well suited to deal with multiphoton absorption and strong fields.

In the study of the H_2^+ molecule, we have formulated two different ways of extracting the kinetic energy spectra: the Virtual Detector Method and the Resolvent Technique for molecules. The Virtual Detector Method was applied in a three-dimensional model for the H_2^+ molecule, and, on the other hand, the Resolvent Technique was extended to be used in molecules, and applied to a two dimensional model for the same molecule. Both methods have advantages and drawbacks. The Virtual Detector Method allows the reduction of the numerical size of our box but it is less accurate than the Resolvent Technique. The latter has the disadvantage of requiring that all the wavefunction is contained in the numerical box, but it can provide very accurate results even to extract above-threshold ionization (ATI) spectra. For the H_2 molecule, since the calculations were performed within a spectral method, the extraction of the spectra was straightfoward.

All these methodologies were developed and used to study molecular processes under ultrashort laser pulses. For the H_2^+ molecule, preliminary results were shown in the three dimensional method, using an XUV pulse where the photon energy and pulse duration were changed, in order to study direct ionization via one-photon absorption. Those results show the validity of the method that is currently being developed in our group.

The extension of the Resolvent Technique was done in the context of this work. With this new

formalism, we were able to extract doubly differential spectra in electronic and nuclear energy, that are of great value to understand the energy sharing between the electron and nuclei in a molecular system. It was applied to study direct ionization, where we were able to explain the main features of the spectra. We also studied the case of a resonant transition between the $1s\sigma_g$ and the $2p\sigma_u$ states. Probably the most interesting case is the observation of the 2D spectrum when a 800 nm laser pulse interacts with the molecule. A regime transition was observed at $E_e \sim 2U_p$. This transition was explained by a simple classical model that states that the horizontal fringes observed in the spectrum are due to direct electrons and the tilted ones are the result of the rescattering of the electron by the nuclei.

Within a spectral method, the study of the autoionization decay of the H_2 molecule was done using an APT-pump-IR-probe scheme. It was shown that the autoionization dynamics can be easily followed by looking at the variation of the 2D spectrum with the time delay between the pulses. The proton kinetic energy spectra show a strong influence of autoionization, which is responsible for the protons that are ejected with energies between 1-6 eV. We have also considered the case, not shown in this report, of a more complicated (APT+IR)-pump-IR-probe scheme to study optically forbidden states. These schemes have proved to be a useful tool to track autoionization dynamics in molecules.

As future work, we plan to include the Resolvent Technique in the three-dimensional model. The use of a hybrid method that combines the Virtual Detector Method and the Resolvent Technique can provide the best of the two worlds. We plan to study in the full-dimensional case the regime transition found in the two-dimensional method when an IR pulse irradiates the H_2^+ molecule. This can reveal some new physics in multiphoton processes.

The study of autoionization that was presented in this masters thesis lead to a publication [21], and the case where optically forbidden resonant states where studied is also submitted [22]. The work done with the Resolvent Technique is currently in preparation for publication [12].

Appendix A

Derivatives in an inhomogeneous grid

Here we derive a five-point formula for the derivative in a inhomogeneous grid. We will define the central point as i and the four adjacent points as

$$i + \nu \qquad i + \beta \qquad i \qquad i + \alpha \qquad i + \mu. \tag{A.1}$$

The Taylor expansion at a point $x + \Delta x$ is

$$f(x + \Delta x) = f(x) + \Delta x f'(x) + \frac{\Delta x^2}{2!} f''(x) + \frac{\Delta x^3}{3!} f'''(x) + \mathcal{O}(\Delta x^4), \tag{A.2}$$

and if $f_\alpha \equiv f(x + \alpha)$ then we can express the expansions (A.2) at points (A.1) as a matrix,

$$\begin{bmatrix} \begin{array}{c|cccc} - & f & f' & f'' & f''' \\ \hline f_\alpha & 1 & \alpha & \alpha^2/2 & \alpha^3/6 \\ f_\beta & 1 & \beta & \beta^2/2 & \beta^3/6 \\ f_\mu & 1 & \mu & \mu^2/2 & \mu^3/6 \\ f_\nu & 1 & \nu & \nu^2/2 & \nu^3/6 \end{array} \end{bmatrix} \tag{A.3}$$

After some algebra we arrive to

$$f' = \frac{\left(\beta^3 - \alpha^3\right)\left(f_\nu - f_\mu\right) - \left(\nu^3 - \mu^3\right)\left(f_\beta - f_\alpha\right)}{\left(\beta^3 - \alpha^3\right)\left(\nu - \mu\right) - \left(\nu^3 - \mu^3\right)\left(\beta - \alpha\right)}. \tag{A.4}$$

Defining $\gamma \equiv \left(\nu^3 - \mu^3\right) / \left(\beta^3 - \alpha^3\right)$ we will have

$$f' = \frac{\left(f_\nu - f_\mu\right) - \gamma\left(f_\beta - f_\alpha\right)}{\left(\nu - \mu\right) - \gamma\left(\beta - \alpha\right)}. \tag{A.5}$$

Appendix B

Particle under a time-dependent electric field

Suppose that a point particle with a initial velocity $\boldsymbol{v}(t_0)$, mass m and charge q, is exposed to a time-dependent electric field, without spatial dependence $\boldsymbol{E}(t)$. In this way we can define the vector potential that is given by

$$\boldsymbol{E}(t) = -\partial_t \boldsymbol{A}(t). \tag{B.1}$$

The second Newton equation is

$$m\dot{\boldsymbol{v}}(t) = q\boldsymbol{E}(t) \tag{B.2}$$

and integrating the equation of motion

$$\boldsymbol{v}(t) = \boldsymbol{v}(t_0) + \frac{q}{m}\int_{t_0}^{t} -\partial_t \boldsymbol{A}(t')\,dt' = \boldsymbol{v}(t_0) + \frac{q}{m}\left[-\boldsymbol{A}(t) + \boldsymbol{A}(t_0)\right]. \tag{B.3}$$

For an electron (in atomic units), $m = 1$ and $q = -1$, so

$$\boldsymbol{v}(t) = \boldsymbol{v}(t_0) + \left[\boldsymbol{A}(t) - \boldsymbol{A}(t_0)\right]. \tag{B.4}$$

We are interested in the final velocity of the electron. If $\boldsymbol{A}(\infty) = 0$ we have that

$$\boldsymbol{v}(\infty) = \boldsymbol{v}(t_0) - \boldsymbol{A}(t_0). \tag{B.5}$$

This correction must be done if we want to measure an electron's velocity when the electric pulse is still present.

Bibliography

[1] P. A. Franken, A. E. Hill, C. W. Peters, and G. Weinreich. Generation of optical harmonics. *Phys. Rev. Lett.*, 7:118–119, Aug 1961.

[2] Ahmed H. Zewail. *Femtochemistry - Atomic-scale dynamics of the chemical bond using ultra-fast lasers.* Nobel Lecture in Chemistry, December 1999.

[3] P. B. Corkum. Plasma perspective on strong field multiphoton ionization. *Phys. Rev. Lett.*, 71:1994–1997, Sep 1993.

[4] M. Lewenstein, Ph. Balcou, M. Yu. Ivanov, Anne L'Huillier, and P. B. Corkum. Theory of high-harmonic generation by low-frequency laser fields. *Phys. Rev. A*, 49:2117–2132, Mar 1994.

[5] R. Kienberger, M. Hentschel, M. Uiberacker, Ch. Spielmann, M. Kitzler, A. Scrinzi, M. Wieland, Th. Westerwalbesloh, U. Kleineberg, U. Heinzmann, M. Drescher, and F. Krausz. Steering attosecond electron wave packets with light. *Science*, 297(5584):1144–1148, 2002.

[6] E. Goulielmakis, M. Uiberacker, R. Kienberger, A. Baltuska, V. Yakovlev, A. Scrinzi, Th. Westerwalbesloh, U. Kleineberg, U. Heinzmann, M. Drescher, and F. Krausz. Direct measurement of light waves. *Science*, 305(5688):1267–1269, 2004.

[7] R Kienberger, E Goulielmakis, M Uiberacker, A Baltuska, V Yakovlev, F Bammer, A Scrinzi, T Westerwalbesloh, U Kleineberg, U Heinzmann, M Drescher, and F Krausz. Atomic transient recorder. *NATURE*, 427(6977):817–821, FEB 26 2004.

[8] J Itatani, J Levesque, D Zeidler, H Niikura, H Pepin, JC Kieffer, PB Corkum, and DM Villeneuve. Tomographic imaging of molecular orbitals. *NATURE*, 432(7019):867–871, DEC 16 2004.

[9] ATJB Eppink and DH Parker. Velocity map imaging of ions and electrons using electrostatic lenses: Application in photoelectron and photofragment ion imaging of molecular oxygen. *REVIEW OF SCIENTIFIC INSTRUMENTS*, 68(9):3477–3484, SEP 1997.

[10] J Ullrich, R Moshammer, A Dorn, R Dörner, L Ph H Schmidt, and H Schmidt-Böcking. Recoil-ion and electron momentum spectroscopy: reaction-microscopes. *Reports on Progress in Physics*, 66(9):1463, 2003.

[11] F. Catoire and H. Bachau. Extraction of the absolute value of the photoelectron spectrum probability density by means of the resolvent technique. *Phys. Rev. A*, 85:023422, Feb 2012.

[12] R. E. F. Silva, F. Catoire, P. Rivière, H. Bachau, and F. Martín. *in preparation.*

[13] A. Palacios, H. Bachau, and F. Martin. Excitation and ionization of molecular hydrogen by ultrashort vuv laser pulses. *Phys. Rev. A*, 75:013408, Jan 2007.

[14] A. Palacios, H. Bachau, and F. Martin. Enhancement and control of h_2 dissociative ionization by femtosecond vuv laser pulses. *Phys. Rev. Lett.*, 96:143001, Apr 2006.

[15] José Luis Sanz-Vicario, Henri Bachau, and Fernando Martín. Time-dependent theoretical description of molecular autoionization produced by femtosecond xuv laser pulses. *Phys. Rev. A*, 73:033410, Mar 2006.

[16] J.F. Pérez-Torres P. Rivière, A. Palacios and F. Martín. *Progress in Ultrafast Intense Laser Science*, volume 8, chapter Probing electron dynamics in simple molecules with attosecond pulses. Springer Frankfurt, 2012.

[17] Alberto González Castrillo. Visualizing, tracing and controlling ultrafast molecular dynamics of single and doubly excited states of h_2. Master's thesis, Universidad Autónoma de Madrid, 2011.

[18] Alicia Palacios. *Ionización y disociación de H_2^+ y H_2 por pulsos láser ultracortos en la región XUV*. PhD thesis, Universidad Autónoma de Madrid, 2006.

[19] Jhon Freddy Pérez-Torres. *Photoionization of the hydrogen molecule using attosecond laser pulses*. PhD thesis, Universidad Autónoma de Madrid, 2006.

[20] Jorge Fernández Hernández. *Dissociative and non dissociative ionization of H_2^+, HeH and H_2 molecules by photons and fast particles*. PhD thesis, Universidad Autónoma de Madrid, 2006.

[21] R. E. F. Silva, P. Rivière, and F. Martín. Autoionizing decay of h$_2$ doubly excited states by using xuv-pump–infrared-probe schemes with trains of attosecond pulses. *Phys. Rev. A*, 85:063414, Jun 2012.

[22] P. Rivière, R. E. F. Silva, and F. Martín. A pump-probe scheme to study the autoionization decay of optically-forbidden h2 doubly excited states. *Journal of Physical Chemistry A, submitted.*

[23] Claude Cohen-Tannoudji, Jaques Dupont-Roc, and Gilbert Grynberg. *Photons and Atoms: Introduction to Quantum Electrodynamics*. Wiley Professional, 1997.

[24] Gilbert Grynberg, Alain Aspect, and Claude Fabre. *Introduction to Quantum Optics: From the Semi-classical Approach to Quantized Light*. Cambridge University Press, 2010.

[25] Martin Winter, Rudiger Schmidt, and Uwe Thumm. Multidimensional quantum-beat spectroscopy: Towards the complete temporal and spatial resolution of the nuclear dynamics in small molecules. *Phys. Rev. A*, 80:031401, Sep 2009.

[26] M Winter, R Schmidt, and U Thumm. Quantum-beat analysis of the rotational-vibrational dynamics in d$_2^+$. *New Journal of Physics*, 12(2):023020, 2010.

[27] Fatima Anis and B. D. Esry. Role of nuclear rotation in dissociation of H$_2^+$ in a short laser pulse. *Phys. Rev. A*, 77:033416, Mar 2008.

[28] R. Dörner, V. Mergel, O. Jagutzki, L. Spielberger, J. Ullrich, R. Moshammer, and H. Schmidt-Böcking. Cold target recoil ion momentum spectroscopy: a momentum microscope to view atomic collision dynamics. *Physics Reports*, 330(2-3):95 – 192, 2000.

[29] J Ullrich, R Moshammer, A Dorn, R Dörner, L Ph H Schmidt, and H Schmidt-Böcking. Recoil-ion and electron momentum spectroscopy: reaction-microscopes. *Reports on Progress in Physics*, 66(9):1463, 2003.

[30] A. Galindo and P. Pascual. *Quantum Mechanics I*. Springer-Verlag, 1990.

[31] D. Scholz and M. Weyrauch. A note on the zassenhaus product formula. *Journal of Mathematical Physics*, 47(3):033505, March 2006.

[32] M. W. J. Bromley and B. D. Esry. Classical aspects of ultracold atom wave packet motion through microstructured waveguide bends. *Phys. Rev. A*, 69:053620, May 2004.

[33] Bernold Feuerstein and Uwe Thumm. On the computation of momentum distributions within wavepacket propagation calculations. *Journal of Physics B: Atomic, Molecular and Optical Physics*, 36(4):707, 2003.

[34] David J. Tannor. *Introduction to Quantum Mechanics, a time-dependent perspective*. University Science Books, 2007.

[35] Morten Forre and Henri Bachau. Orientation effects in the coulomb-explosion ionization of an H_2^+ wave packet by short xuv pulses: Applicability of the fixed-nuclei approximation. *Phys. Rev. A*, 77:053415, May 2008.

[36] K. J. Schafer and K. C. Kulander. Energy analysis of time-dependent wave functions: Application to above-threshold ionization. *Phys. Rev. A*, 42:5794–5797, Nov 1990.

[37] H. G. Muller. Numerical simulation of high-order above-threshold-ionization enhancement in argon. *Phys. Rev. A*, 60:1341–1350, Aug 1999.

[38] H. G. Muller and F. C. Kooiman. Bunching and focusing of tunneling wave packets in enhancement of high-order above-threshold ionization. *Phys. Rev. Lett.*, 81:1207–1210, Aug 1998.

[39] F. Catoire, C. Blaga, E. Sistrunk, H. Muller, P. Agostini, and L. DiMauro. Mid-infrared strong field ionization angular distributions. *Laser Physics*, 19:1574–1580, 2009. 10.1134/S1054660X09150079.

[40] Bernold Feuerstein and Uwe Thumm. Fragmentation of h_2^+ in strong 800-nm laser pulses: Initial-vibrational-state dependence. *Phys. Rev. A*, 67:043405, Apr 2003.

[41] W. Becker, F. Grasbon, R. Kopold, D.B. Milosevic, G.G. Paulus, and H. Walther. Above-threshold ionization: From classical features to quantum effects. volume 48 of *Advances In Atomic, Molecular, and Optical Physics*, pages 35 – 98. Academic Press, 2002.

[42] Lucjan Piela. *Ideas of Quantum Chemistry*. Elsevier, 2007.

[43] U. Fano. Effects of configuration interaction on intensities and phase shifts. *Phys. Rev.*, 124:1866–1878, Dec 1961.

[44] Herman Feshbach. Unified theory of nuclear reactions. *Annals of Physics*, 5(4):357 – 390, 1958.

[45] P. Johnsson, J. Mauritsson, T. Remetter, A. L'Huillier, and K. J. Schafer. Attosecond control of ionization by wave-packet interference. *Phys. Rev. Lett.*, 99:233001, Dec 2007.

[46] Paula Rivière, Olaf Uhden, Ulf Saalmann, and Jan M Rost. Strong field dynamics with ultrashort electron wave packet replicas. *New Journal of Physics*, 11(5):053011, 2009.

[47] X. M. Tong, P. Ranitovic, C. L. Cocke, and N. Toshima. Mechanisms of infrared-laser-assisted atomic ionization by attosecond pulses. *Phys. Rev. A*, 81:021404, Feb 2010.

[48] G. Sansone, F. Kelkensberg, J. F. Perez-Torres, F. Morales, M. F. Kling, W. Siu, O. Ghafur, P. Johnsson, M. Swoboda, E. Benedetti, F. Ferrari, F. Lepine, J. L. Sanz-Vicario, S. Zherebtsov, I. Znakovskaya, A. L'Huillier, M. Yu. Ivanov, M. Nisoli, F. Martin, and M. J. J. Vrakking. Electron localization following attosecond molecular photoionization. *NATURE*, 465(7299):763–U3, JUN 10 2010.